

Cite this: *Chem. Sci.*, 2020, **11**, 4648

All publication charges for this article have been paid for by the Royal Society of Chemistry

Structural properties of ultra-small thorium and uranium dioxide nanoparticles embedded in a covalent organic framework†

Liane M. Moreau, ^{‡,a} Alexandre Herve, ^{‡,a} Mark D. Straub, ^{ab} Dominic R. Russo, ^{ab} Rebecca J. Abergel, ^{ab} Selim Alayoglu, ^a John Arnold, ^{ab} Augustin Braun, ^a Gauthier J. P. Deblonde, ^{§,a} Yangdongling Liu, ^a Trevor D. Lohrey, ^{ab} Daniel T. Olive, ^{ac} Yusen Qiao, ^{ad} Julian A. Rees, ^a David K. Shuh, ^a Simon J. Teat, ^a Corwin H. Booth ^{*,a} and Stefan G. Minasian ^{*,a}

We report the structural properties of ultra-small ThO_2 and UO_2 nanoparticles (NPs), which were synthesized without strong binding surface ligands by employing a covalent organic framework (COF-5) as an inert template. The resultant NPs were used to observe how structural properties are affected by decreasing grain size within bulk actinide oxides, which has implications for understanding the behavior of nuclear fuel materials. Through a comprehensive characterization strategy, we gain insight regarding how structure at the NP surface differs from the interior. Characterization using electron microscopy and small-angle X-ray scattering indicates that growth of the ThO_2 and UO_2 NPs was confined by the pores of the COF template, resulting in sub-3 nm particles. X-ray absorption fine structure spectroscopy results indicate that the NPs are best described as ThO_2 and UO_2 materials with unpassivated surfaces. The surface layers of these particles compensate for high surface energy by exhibiting a broader distribution of Th–O and U–O bond distances despite retaining average bond lengths that are characteristic of bulk ThO_2 and UO_2 . The combined synthesis and physical characterization efforts provide a detailed picture of actinide oxide structure at the nanoscale, which remains highly underexplored compared to transition metal counterparts.

Received 4th December 2019
Accepted 13th April 2020

DOI: 10.1039/c9sc06117g
rsc.li/chemical-science

Introduction

Actinide chemistry at the nanoscale has become of increased importance due to the potential for improved safety and efficiency with decreasing grain size in advanced nuclear fuels.^{1–3} For example, self-heating of nuclear fuel⁴ following loss of coolant may be lessened by employing advanced reactor fuels with characteristics similar to the UO_2 high burn-up structure (HBS), in which UO_2 fuel evolves into a hierarchical, mesoporous material with 1 μm pores distributed throughout a nanocrystalline UO_2 solid.^{1,5,6} Actinide nanoparticles are also known to play a major role in the migration of radionuclides

through environmental systems,^{7–11} and have been proposed as agents for targeted alpha-therapy,^{12–17} and for applications in thermopower¹⁸ and heterogeneous catalysis.^{19–24} Further innovation in these areas will require methods to synthesize and characterize actinides at the nanoscale, an area that is relatively unexplored and beyond current predictive capabilities. For stable d-block metals, it has been well-established that as grain size is reduced to the nanoscale in discrete particles certain electronic, magnetic, and chemical phenomena may emerge that do not occur in bulk solids or in molecular systems. This behavior can be traced directly to factors that are intrinsic to nanoparticles including changes in structural order, larger surface energies and surface area-to-volume ratios, and quantization of the electronic states.^{25–29} By comparison, the chemistry of actinide nanoparticle systems is underdeveloped,^{30,31} and there is little evidence for intrinsic size effects on phase stabilities, surface reactivities, and 5f-electron behavior.^{32–36} Handling the actinide elements has also posed challenges, as hazards associated with radioactivity mandate special procedures for containment, while requirements for waste minimization, isotope recovery, and reuse necessitate small-scale reactions that are incompatible with most nanoparticle synthesis and characterization methods.³⁷ Efforts to move

^aLawrence Berkeley National Laboratory, Berkeley, CA 94720, USA. E-mail: chbooth@lbl.gov; sgminasian@lbl.gov

^bUniversity of California, Berkeley, CA 94720, USA

^cLos Alamos National Laboratory, Los Alamos, NM 87545, USA

^dUniversity of Pennsylvania, Philadelphia, PA 19104, USA

† Electronic supplementary information (ESI) available. CCDC 1952481 and 1952482. For ESI and crystallographic data in CIF or other electronic format see DOI: 10.1039/c9sc06117g

‡ These authors contributed equally.

§ Current Address: Lawrence Livermore National Laboratory, Livermore, CA 94550, USA.



beyond the actinide electronic structure models developed for ideal molecular systems³⁸ or extended solids^{39–43} and towards three-dimensional nanoscale materials require synthetic methodologies for actinide nanoparticles that meet these technical requirements while retaining the high degree of size and composition control provided by conventional colloidal chemistry approaches.

Recent developments in inorganic synthesis and increased understanding of environmental colloids have provided new opportunities to explore the chemistry of actinides at the nanoscale.^{44–53} Molecular cluster chemistry of the tetravalent actinides, exemplified by a class of actinide oxo hydroxide clusters,^{54–66} has provided valuable structural insight into the growth of bulk AnO_2 (An = actinide) by the controlled hydrolysis of molecular precursors. Synthetic techniques for actinide nanoparticles have also been reported that include direct decomposition of actinide precursors into nanoparticles in aqueous solutions by irradiation,^{2,8,67} sonolysis^{68,69} or *via* hydrothermal approaches.^{70,71} These latter methods often result in nonuniform size distributions and less desirable aggregated particles; however, control over particle size has been effectively achieved by incorporating surfactants into the reaction mixture. For instance, size-controlled syntheses have been reported for a range of anisotropic and isotropic actinide oxide nanoparticles (An = Th, U, Np, Pu) by thermal decomposition of molecular precursors in the presence of organic ligands.^{18,72–76} Unfortunately, the use of surfactant molecules also complicates comparisons to analogous bulk materials. For example, surface ligands have been shown to directly alter nanoparticle surface charge and electronic structure,^{77–79} as well as shape and surface reconstruction,⁸⁰ while also impacting their functionality in catalysis^{81–83} and luminescence properties.^{84–86} Hence, it has remained difficult to identify changes in physical behavior that are a direct consequence of particle size, particularly in ultra-small nanoparticles where surface speciation is a major and sometimes dominant component of the overall composition. Such factors become critical when studying how the effects of decreasing grain size may affect extended solids.

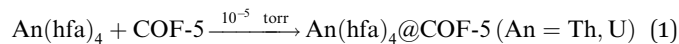
Towards this end, porous frameworks provide a templated pathway to synthesize monodisperse nanoparticles that avoids the complication of surface ligands through size-confinement of nanoparticles to the template pore size. Recent efforts to adapt earlier template-directed syntheses that use metal-organic frameworks (MOFs)^{87,88} and covalent organic frameworks (COFs) have been reviewed^{89–91} and include successful syntheses of Pd,^{89,92–94} Pt,^{93,95} Ag,⁹⁶ and Au nanoparticles.^{97,98} COF-5 in particular is chemically and thermally robust, having been assembled from strong covalent bonds between B, C, and O.⁹⁹ Hence, COF-5 could potentially accommodate a wide range of precursors and decomposition conditions, and permit rational tuning of the molecular coordination chemistry and decomposition mechanisms. Customizing a template-directed synthesis approach for sub-milligram scale, solvent-free reactions could enable studies of radioactive actinide nanoparticles by minimizing the amount of metal needed and radioactive waste generated.

Herein, we report the synthesis and detailed structural characterization of ultra-small ThO_2 and UO_2 nanoparticles (NPs) without the use of surface ligands by using COF-5 as a size-directing template and tetravalent thorium and uranium hexafluoroacetylacetone (hfa) complexes as precursors ($\text{Th}(\text{hfa})_4$ and $\text{U}(\text{hfa})_4$). A comprehensive characterization toolbox was developed to trace the synthetic process, understand precursor decomposition, and compare both the nanoscale structural properties with bulk actinide oxide structure and the implications of structural differences on nuclear fuel materials. Additionally, such an approach was required in order to determine the nanoparticle composition, which is not possible using conventional techniques typically used in nanoparticle characterization including transmission electron microscopy (TEM) and X-ray diffraction (XRD). Chemical imaging and spectroscopic analyses of the synthetic products revealed a controlled process involving nanoparticle formation without degradation of the COF-5 template. Nanoparticle sizes were evaluated with TEM and small-angle X-ray scattering (SAXS) techniques, which show that nanoparticle growth was effectively limited by the size of COF-5 pores such that ultra-small nanoparticle products (<3 nm) were obtained. A thorough X-ray absorption fine structure (XAFS) spectroscopy study shows that the nanoparticles are best formulated as tetravalent ThO_2 and UO_2 with disordered cubic fluorite crystalline structures. The XAFS data also show that there are no strong interactions between the nanoparticle surface and organic ligands or the COF host. Rather, the chemistry of these ThO_2 and UO_2 nanoparticles can be more directly compared to their bulk counterparts, and enable us to consider implications of the nanoparticle surface characteristics on the performance of nanostructured nuclear fuels.

Results

Synthesis of COF-5 inclusion compounds

Formation of the $\text{Th}(\text{hfa})_4@\text{COF-5}$ and $\text{U}(\text{hfa})_4@\text{COF-5}$ inclusion compounds was achieved *via* room-temperature sublimation under static vacuum of $\text{Th}(\text{hfa})_4$ or $\text{U}(\text{hfa})_4$ precursors from glass vials into an activated COF-5 host material that was in the same flask but contained within a separate, open vial (eqn (1)).



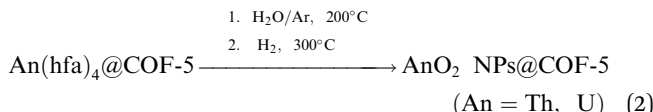
During this process, formation of the inclusion compounds was accompanied by a visible and measurable mass loss of the precursor and corresponding mass gain for the COF-5 host. The otherwise colorless COF-5 starting material also adopted some visible characteristics of the $\text{U}(\text{hfa})_4$ precursor (brown) upon formation of $\text{U}(\text{hfa})_4@\text{COF-5}$ (tan). Predictably, no significant color change was observed upon exposure of COF-5 to $\text{Th}(\text{hfa})_4$, which is colorless. Sublimation consistently provided high and homogenous loading of the precursors in the COF-5 host when compared with solution phase loading. Using the uranium case as an example, multiple syntheses of $\text{U}(\text{hfa})_4@\text{COF-5}$ by exposure of excess $\text{U}(\text{hfa})_4$ to COF-5 achieved loadings of 90% of



the theoretical maximum for COF-5 (based on the pore volume of COF-5 and the crystallographic density of $\text{U}(\text{hfa})_4$).⁹⁹ At such high loadings, the $\text{U}(\text{hfa})_4@\text{COF-5}$ material was 63% precursor by mass (64% for $\text{Th}(\text{hfa})_4@\text{COF-5}$). Inclusion compounds formed with this maximal loading were used in all the subsequent decomposition reactions and characterization studies described below. Placing $\text{Th}(\text{hfa})_4@\text{COF-5}$ or $\text{U}(\text{hfa})_4@\text{COF-5}$ under active vacuum at elevated temperature resulted in a mass loss and color change that was consistent with removal of the precursor molecules and recovery of pure COF-5. The precursor molecules could also be removed readily by washing the inclusion compounds with diethyl ether. Taken together with the imaging and spectroscopy results described below, these data show that formation of the inclusion compounds was a reversible process that did not result in a change in composition or structure for the precursor molecules or the COF-5 host.

Decomposition of COF-5 inclusion compounds

Decomposition of the $\text{Th}(\text{hfa})_4@\text{COF-5}$ and $\text{U}(\text{hfa})_4@\text{COF-5}$ inclusion compounds was achieved in the solid state *via* exposure to a gaseous mixture of H_2O in Ar at 200 °C with rigorous exclusion of O_2 . Under these anaerobic but humid conditions, a pure sample of COF-5 was not significantly degraded at temperatures reaching 300 °C based on analysis by powder X-ray diffraction and infrared spectroscopy. Subsequent evacuation at 10^{-5} torr to remove organic byproducts and undecomposed precursors resulted in formation of new dark gray materials. An additional step involving heating at 300 °C in an atmosphere of pure H_2 was introduced under the initial assumption that higher oxides may be present. While this step functions effectively to anneal the nanoparticles and increase product crystallinity, subsequent characterization indicates that it is not necessary to reduce higher oxides formed during the initial decomposition with H_2O in Ar (Fig. S21†). Mass losses of approximately 45–50% were observed upon weighing, which shows that precursor decomposition and elimination of the organic hfa ligands was achieved selectively, resulting in formation of new actinide oxide products without detectable decomposition of the COF-5 host material (eqn (2)).



At this point, to simplify the following discussion, these materials are formulated as ThO_2 NPs@COF-5 and UO_2 NPs@COF-5; however, note that the binary dioxide composition was only determined as the most appropriate structural description through the additional experiments described below. The reaction pathway leading to formation of AnO_2 NPs@COF-5 is hypothesized to proceed *via* protonolysis of the $\text{An}(\text{hfa})_4$ precursors and formation of intermediate hydroxide species, followed by condensation to ThO_2 or UO_2 . However, $\text{Th}(\text{OH})_4$ and $\text{U}(\text{OH})_4$ are not known, and closely related Th^{4+} and U^{4+} oxo hydroxide clusters^{63,100} may be more plausible

intermediates. Testing these hypotheses is the subject of ongoing investigation.

Powder X-ray diffraction

Fig. 1 shows powder X-ray diffraction (PXRD) patterns for COF-5, the inclusion compounds $\text{Th}(\text{hfa})_4@\text{COF-5}$ and $\text{U}(\text{hfa})_4@\text{COF-5}$, and nanoparticle composites ThO_2 NPs@COF-5 and UO_2 NPs@COF-5. It should be noted that for PXRD and all subsequent characterization methods, the nanoparticles remained confined to the COF-5 template. The particles were not removed from the template in order to prevent any structural changes or aggregation that might alter their resulting morphology and properties. Reflections that are characteristic of guest-free COF-5 are observed at the same position for each of the inclusion compounds and nanoparticle composites. The close correspondence with COF-5 suggests that the framework

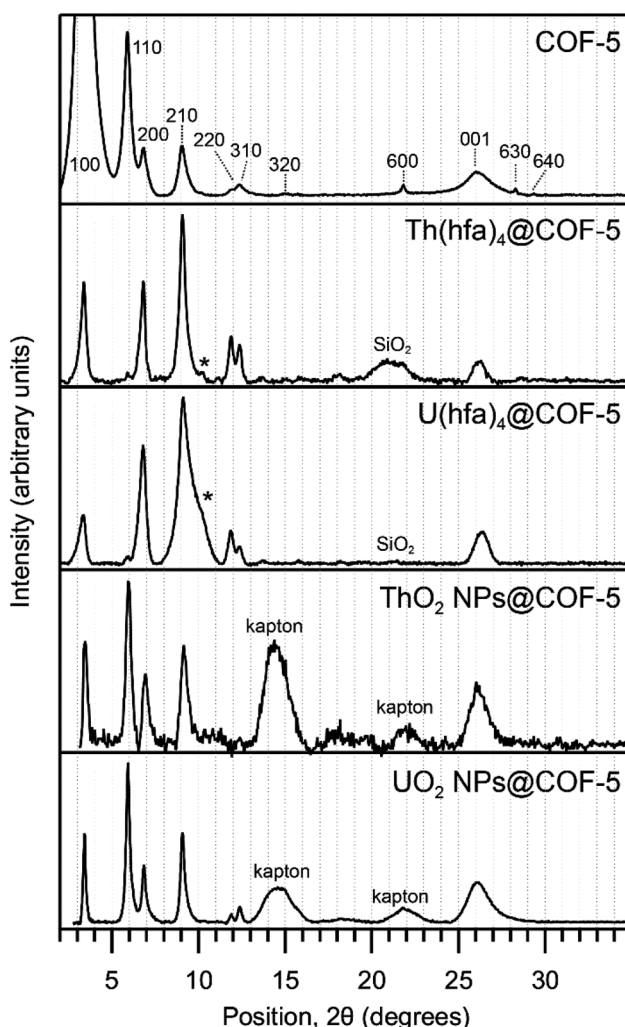


Fig. 1 PXRD patterns of COF-5, inclusion compounds and NPs@COF-5. All patterns are normalized to the 110 or 210 reflection, whichever was more intense, to emphasize changes in the relative intensities of weaker reflections. Reflections indicated with an asterisk (*) correspond to an ordering of the incorporated $\text{Th}(\text{hfa})_4$ or $\text{U}(\text{hfa})_4$ molecules.



composition and structure remained intact throughout the synthetic process. The inclusion compounds and nanoparticle composites data do not exhibit changes in the (001) reflection associated with altered stacking behavior,¹⁰¹ nor are changes observed in the COF-5 reflections consistent with hydrolysis from exposure to small amounts of H₂O during the synthetic process.¹⁰² The lack of peak broadening or angular shifts suggests no strong host–guest bonding interactions occurred with the precursor molecules or nanoparticle surfaces, which would have resulted in strain or modification of COF-5 functional groups.¹⁰³ One weak reflection is observed near 10° 2θ in each pattern for Th(hfa)₄@COF-5 and U(hfa)₄@COF-5 that is attributed to the Th(hfa)₄ or U(hfa)₄ molecules. Such reflections could arise from ordering of the guest molecules in the COF-5 channels or from trace amounts of unincorporated, crystalline Th(hfa)₄ or U(hfa)₄. Reflections corresponding to ThO₂ or UO₂ are not identified in the patterns of ThO₂ NPs@COF-5 or UO₂ NPs@COF-5, and are presumed to be broadened into the baseline. Although Scherrer analysis of the particle size is therefore precluded, such an observation is consistent with the exceptionally small nanoparticle sizes determined using X-ray scattering (see section below).

Compared to COF-5, intensities for the first two low-angle reflections (100 and 110) are inverted relative to the remaining reflections. As has been observed previously in related inclusion compounds and nanoparticle composite materials,¹⁰⁴ inversion of the low-angle reflections is characteristic of the presence of absorbed and disordered guest materials within the host.¹⁰⁵ The effect is particularly pronounced for the inclusion compounds Th(hfa)₄@COF-5 and U(hfa)₄@COF-5, which had greater mass fractions of guest material. Upon decomposition to ThO₂ NPs@COF-5 and UO₂ NPs@COF-5, the relative intensity of the 100 and 110 reflections is partially restored, which provides further support for elimination of ligand byproducts resulting in a lowered pore guest occupancy. Alternatively, PXRD patterns obtained following removal of the precursor molecules indicate

recovery of pure COF-5. Taken together, these observations are consistent with the decomposition pathway involving reversible absorption of Th(hfa)₄ and U(hfa)₄ inside the COF-5 pores, followed by selective decomposition to ThO₂ and UO₂ nanoparticles without detectable structural degradation of the COF-5 host that would be expected from strong host–guest interactions, or hydrolysis at elevated temperature.

Transmission electron microscopy

ThO₂ NPs@COF-5 and UO₂ NPs@COF-5 materials were investigated using transmission electron microscopy (TEM) to determine whether ThO₂ NPs@COF-5 and UO₂ NPs@COF-5 were successfully synthesized during the decomposition reactions. Bright and dark field TEM images (Fig. 2) show a roughly isotropic distribution of quasi-spherical nanoparticles throughout the greater COF-5 particles and confirm high particle loading. Digitally measured size analysis of 100 nanoparticles per sample in thinner regions suggests that the average particle diameter was 2.4 ± 0.5 nm for ThO₂ NPs@COF-5 and 2.7 ± 0.6 nm for UO₂ NPs@COF-5, which indicates that growth for a majority of the nanoparticles was confined by the COF-5 pore size (2.7 nm).⁹⁹ However, due to the varied height of the three dimensional composite inorganic/organic ThO₂ NPs@COF-5 and UO₂ NPs@COF-5 materials and the importance of vertical alignment in image acquisition, as well as the difficulty in imaging sub-3 nm particles,¹⁰⁶ images of incorporated nanoparticles provide only an initial estimate of the upper limit for nanoparticle size. This limitation prompted the use of small angle X-ray scattering to make a more statistically significant size determination (see below). Still, the TEM images provide necessary visual confirmation for the formation of sub-3 nm quasi-spherical nanoparticles within the organic COF matrix.

TEM also provides evidence that the COF-5 template material was not locally destroyed. This appears to be somewhat

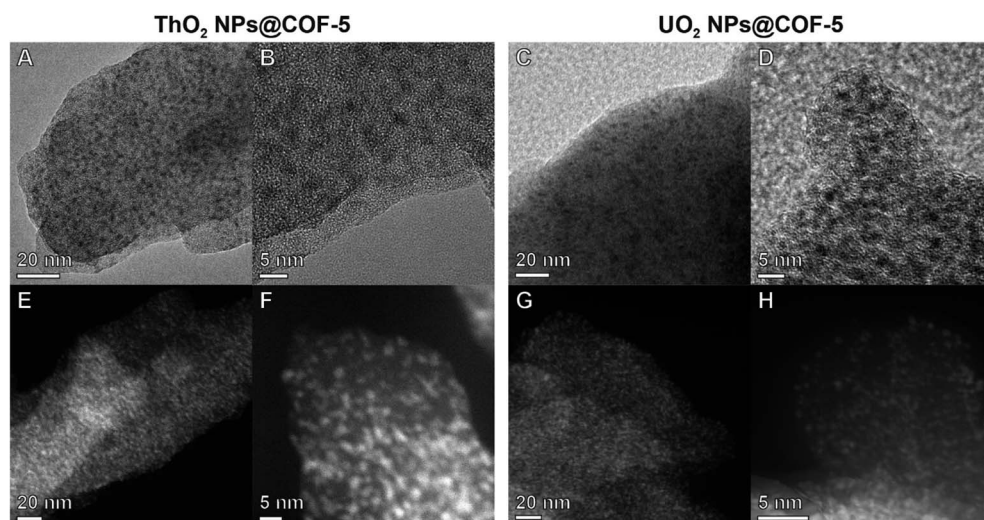


Fig. 2 Bright-field TEM (A–D) and dark-field STEM (E–H) images show nanoparticles on the same size order as the COF pores (2–3 nm) embedded throughout the organic COF template. No discernable difference between ThO₂ (left) and UO₂ (right) NP products is observed.



unique for this NP@COF-5 system, in that similar template-based approaches have observed destruction of the template leading to growth of larger particles.^{92,107} Additionally, while not arranged with consistent inter-particle spacing, the nanoparticles appear to have been confined within the COF-5 interior. This confinement is in contrast to some prior work on templated nanoparticle systems, where migration of nanoparticles to the organic template surface has been observed.¹⁰⁸

Small-angle X-ray scattering

To confirm that ThO_2 and UO_2 nanoparticle growth was constrained by the pore size of the COF-5 host, global statistics of nanoparticle size distributions were also investigated using small-angle X-ray scattering (SAXS). Whereas the average nanoparticle diameters are potentially inaccurate and skewed toward larger particle sizes with TEM because of the ultra-small nanoparticle sizes and the focusing challenges that are a consequence of the uneven height of the three-dimensional COF-5 background, SAXS provides statistically accurate size and polydispersity measurements.^{109,110} SAXS also does not produce the high local heating of TEM, which may result in unwanted sample damage leading to decomposition or sintering of nanoparticle products.¹⁰⁶ In the integrated 1-D SAXS patterns of the NPs@COF-5 constructs (Fig. 3), a form factor is observable in addition to the COF-5 structure at higher q . Features from a form factor (simulated as the blue line in Fig. 3A and B) are absent from patterns of the inclusion compounds and pure COF-5 (see Fig. S5 and S6 in the ESI†), revealing that nanoparticles formed during decomposition and not upon inclusion compound incorporation. The wide-angle X-ray scattering (WAXS) region ($>0.1 \text{ \AA}^{-1}$) is consistent with the PXRD results and shows that the peaks from COF-5 are still present in the patterns of the inclusion compounds and NPs@COF-5 constructs, providing additional evidence that the COF-5 structure was minimally perturbed upon incorporation of guest species. Also like the PXRD, the first order reflection peak associated with COF-5 (Fig. 3A, B, S5 and S6†) is reduced in

intensity when precursor or nanoparticle guests are incorporated, as expected for filled pores.¹⁰⁵

Analysis from fitting the form factor assuming a spherical nanoparticle morphology and Schulz distribution of particle radii results in an average size of $1.36 \pm 0.05 \text{ nm}$ for the UO_2 nanoparticles and $1.62 \pm 0.02 \text{ nm}$ for ThO_2 , with polydispersities of 0.48 and 0.37 respectively, in terms of the polydispersity index (PDI). These PDI values correspond to standard deviations in size that are less than 1 nm, and comparable to the values achieved for colloidally synthesized particles, which are described as uniform. Reported standard deviations in the dimensions of actinide oxide nanoparticles synthesized colloidally range from $0.14\text{--}1.5 \text{ nm}$, independent of average particle size.^{18,21,73\text{--}76} These sizes correspond to 32 U and 51 Th atoms per particle on average when assuming bulk densities. The plotted Schulz distribution of nanoparticle sizes in each of the samples (Fig. 3C) shows that the 2.7 nm diameter pores of the COF-5 template limited nanoparticle growth to the “ultra-small” size regime, where the nanoparticles have an exceptionally high percentage of surface atoms.¹¹¹

Infrared spectroscopy

The Fourier transform infrared (FT-IR) spectra are in accordance with the controlled, two-step nanoparticle synthesis pathway described above. Fig. 4 highlights selected regions in the IR spectra of $\text{Th}(\text{hfa})_4@\text{COF-5}$ and $\text{U}(\text{hfa})_4@\text{COF-5}$, ThO_2 NPs@COF-5 and UO_2 NPs@COF-5, the $\text{Th}(\text{hfa})_4$ and $\text{U}(\text{hfa})_4$ precursors, and guest-free COF-5. Complete spectral details are provided in Table S6 and Fig. S7, S8 of the ESI.† In general, strong correlations are found throughout the entire spectral window between the vibrational frequencies measured for the $\text{Th}(\text{hfa})_4@\text{COF-5}$ and $\text{U}(\text{hfa})_4@\text{COF-5}$ inclusion compounds and their separated COF-5, $\text{Th}(\text{hfa})_4$, or $\text{U}(\text{hfa})_4$ constituents,^{112,113} such that the host and guest fingerprints are effectively superimposed. For example, the $\nu_{\text{C}=\text{C}}$ vibrations associated with COF-5 are observed at 1492 and 1523 cm^{-1} , and at the same energies for $\text{U}(\text{hfa})_4@\text{COF-5}$ and $\text{Th}(\text{hfa})_4@\text{COF-5}$. The two $\nu_{\text{C}=\text{C}}$ bands associated with the hfa ligand at 1534

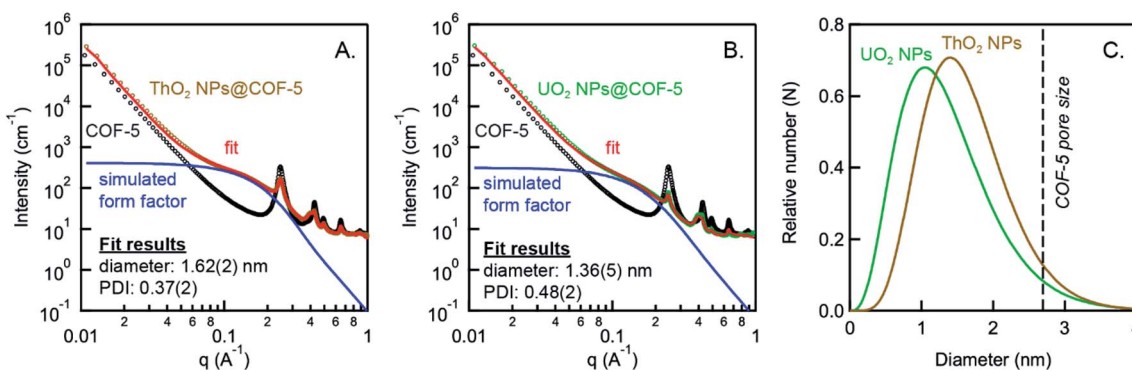


Fig. 3 SAXS results from form factor fitting of NPs@COF-5. The SAXS patterns obtained from ThO_2 NPs@COF-5 (A, tan) and UO_2 NPs@COF-5 (B, green) are well-fit (red) with a spherical form factor (simulated in blue) and background contributions. WAXS peaks in the higher- q region of the patterns reveal that diffraction peaks from COF-5 (black) are retained. (C) NPs@COF-5 size distributions plotted as Schulz distributions extracted from fitting results. It is apparent from comparing these distributions to the 2.7 \AA COF-5 pore size that the particles were confined within the COF-5 pores.



and 1560 cm^{-1} for $\text{U}(\text{hfa})_4$ increase slightly in energy (by 4 to 5 cm^{-1}) upon formation of $\text{U}(\text{hfa})_4@\text{COF-5}$, to 1539 and 1564 cm^{-1} respectively. Meanwhile, the higher energy $\nu_{\text{C}=\text{O}}$ and $\nu_{\text{C}=\text{C}}$ vibrations associated with the hfa ligand are observed at 1612 and 1650 cm^{-1} for pure $\text{U}(\text{hfa})_4$ and similar frequencies of 1621 and 1646 cm^{-1} for $\text{U}(\text{hfa})_4@\text{COF-5}$. Following decomposition and formation of UO_2 NPs@COF-5, all of the $\nu_{\text{C}=\text{O}}$ and $\nu_{\text{C}=\text{C}}$ vibrations that are characteristic of the hfa ligand disappear, while the COF-5 bands at 1492 and 1523 cm^{-1} remain. Similar observations are made throughout the entire spectral window from 500 to 4000 cm^{-1} , and no new transitions were identified in the spectrum of any product that are not also present for the molecular precursors and COF-5 components.

The IR spectra were scrutinized carefully for evidence of a uranyl stretch that would indicate formation of a higher oxide in the sample of UO_2 NPs@COF-5. Uranyl species can exhibit a strong vibration in IR spectra between $900\text{--}1000\text{ cm}^{-1}$,¹¹⁴ however, no such transition can be unambiguously identified in the IR spectra for either $\text{U}(\text{hfa})_4@\text{COF-5}$ or UO_2 NPs@COF-5. Each of the spectra for COF-5, $\text{Th}(\text{hfa})_4@\text{COF-5}$, $\text{U}(\text{hfa})_4@\text{COF-5}$, ThO_2 NPs@COF-5, and UO_2

NPs@COF-5 exhibit a similar weak band at 973 cm^{-1} which was attributed to a $\nu_{\text{C}=\text{C}}$ vibration associated with COF-5. Furthermore, no significant differences in peak energy were observed in IR spectra obtained from samples of UO_2 NPs@COF-5 prepared with ^{18}O labelled water and unlabeled water (Fig. S9 in the ESI†). Taken together, the results show that IR spectroscopy does not provide evidence for a higher oxide containing uranyl in the UO_2 NPs.

Soft X-ray spectromicroscopy

Considering the complex composition and three-dimensional structure of the materials described above, we sought additional insights from soft X-ray spectromicroscopy techniques.¹¹⁵ A scanning transmission X-ray microscope (STXM) was used for imaging, elemental mapping, and C, O, and F K-edge as well as Th and U N_{5,4}-edge X-ray absorption spectroscopy (XAS). Fig. 5, 6 and S10–S12 in the ESI† show images and spectra for $\text{Th}(\text{hfa})_4@\text{COF-5}$, $\text{U}(\text{hfa})_4@\text{COF-5}$, ThO_2 NPs@COF-5, UO_2 NPs@COF-5, and selected reference materials. Micron-sized particles of the low-melting solids $\text{Th}(\text{hfa})_4$ and $\text{U}(\text{hfa})_4$ instantly formed liquid droplets in the X-ray beam that ultimately evaporated during longer exposures, which precluded analysis by STXM-XAS.

The elemental maps shown in Fig. 5 were used to determine the average optical density (OD) in the micron-scale particles. Individual OD values are affected by the mass absorption coefficients, which vary for different elements and absorption edges, and by the surface concentration (density \times thickness) of the absorbing atom, which varies for different compositions and particle sizes. Hence, trends in OD values between datasets were determined by comparing changes in the OD in the fluorine maps (OD_F) relative to the OD in the same target area of the C, O, and Th or U maps (OD_C , OD_O , and OD_{Th} or OD_U). For example, the $\text{OD}_F/\text{OD}_{\text{Th}}$ ratio decreases substantially from 13.2 for $\text{Th}(\text{hfa})_4@\text{COF-5}$ to 0.7 for ThO_2 NPs@COF-5. Similarly, the OD_F/OD_U ratio decreases from 14.9 for $\text{U}(\text{hfa})_4@\text{COF-5}$ to 0.0 for UO_2 NPs@COF-5. These observations are generally consistent with the proposed decomposition pathway involving elimination of fluorinated ligand byproducts and formation of ThO_2 and UO_2 nanoparticles. STXM-XAS measurements were especially sensitive for the detection of fluorine in thicker particles, in part because the COF-5 material does not contain fluorine and also because of the high probability of $\text{F}\ 1\text{s} \rightarrow 2\text{p}$ transitions at the F K-edge. As a result, small amounts of fluorine are observable in the elemental map of ThO_2 NPs@COF-5, and in the F K-edge XAS spectra for both ThO_2 NPs@COF-5 and UO_2 NPs@COF-5 (Fig. S12†), which may reflect the presence of trace actinide fluoride contamination or incomplete elimination of fluorinated byproducts. Fluorine contamination is known to occur during the preparation of lanthanide oxide films by chemical vapor deposition of fluorinated precursors,^{116–121} although this effect has been mitigated by incorporating H_2O gas.¹¹⁶ Under anhydrous conditions, complexes similar to $\text{Th}(\text{hfa})_4$ and $\text{U}(\text{hfa})_4$ also function as single-source precursors for the preparation of lanthanide fluorides.^{122,123}

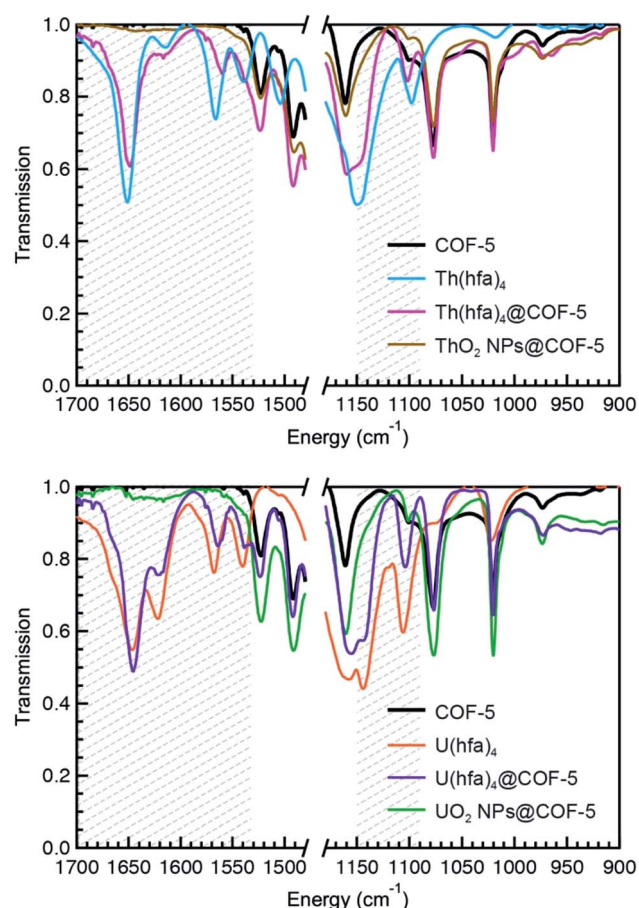


Fig. 4 Selected regions of the FT-IR spectra for COF-5, $\text{Th}(\text{hfa})_4$, $\text{Th}(\text{hfa})_4@\text{COF-5}$, and ThO_2 NPs@COF-5 (top) and COF-5, $\text{U}(\text{hfa})_4$, $\text{U}(\text{hfa})_4@\text{COF-5}$, and UO_2 NPs@COF-5 (bottom) are shown. Portions of the data with a dotted background highlight transitions associated with the hfa ligand, while remaining portions with white backgrounds contain primarily COF-5 based transitions.



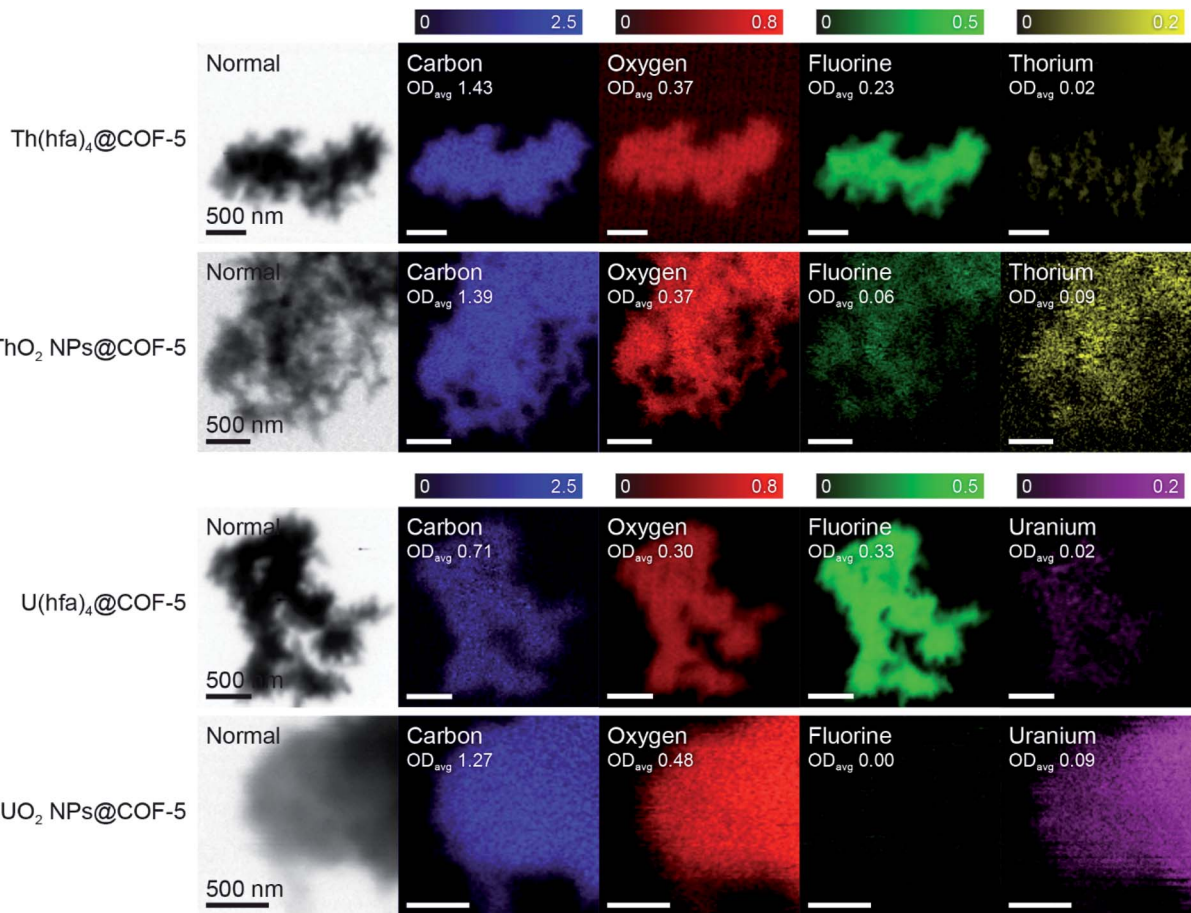


Fig. 5 Representative single-energy contrast images and elemental difference maps of micron-scale COF-5 particles that were used to obtain X-ray absorption spectra. Lighter regions in the elemental maps correspond to greater concentration of the absorbing atom and were obtained by subtraction of two images: one taken at an energy just below the X-ray absorption edge and another taken at the absorption maximum. Because the transmission pathlength is governed by the thickness of each selected particle, which varies between datasets, only relative (as opposed to absolute) intensities should be compared between samples (see text). To facilitate comparisons, each set of four elemental maps is presented on a common optical density scale that is provided at the head of the column. The indicated average optical density values (OD_{avg}) were determined by averaging the optical density at each pixel in particle-containing regions of the maps. Analyses were conducted on target areas greater than $1\ \mu\text{m}^2$ with 5000 or more pixels and were repeated on many individual particles.

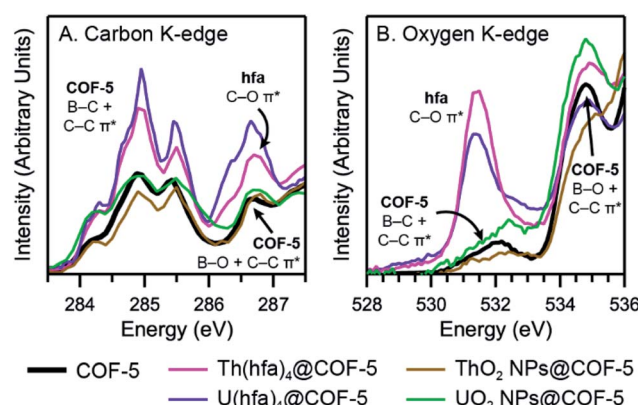


Fig. 6 Plots comparing the C K-edge (A) and O K-edge (B) XAS for $\text{Th}(\text{hfa})_4@\text{COF-5}$, $\text{U}(\text{hfa})_4@\text{COF-5}$, ThO_2 NPs@COF-5, and UO_2 NPs@COF-5. Feature assignments were derived by comparisons with data reported previously for pure COF-5 and acetylacetone,¹²⁴ as well as reference samples $\text{Na}(\text{hfa})$, $\text{Th}(\text{hfa})_4$, and $\text{U}(\text{hfa})_4$ (Fig. S10–S12 in the ESI†).

Attempts to image the 1–3 nm nanoparticles using STXM exceeded the focusing ability of the X-ray optic, which provided a typical spatial resolution of 35–40 nm. However, STXM accommodated larger and thicker COF-5 particles than the TEM experiments and was more effective for probing micron-scale morphology. For each of the products, the STXM images show similar tight micron-scale aggregates of smaller COF-5 particles and homogenous elemental compositions on the micron scale. This determination was reached following surveys of a large number of particles that were analyzed in multiple independent samples and over multiple beam-runs.

A qualitative analysis of the C and O K-edge XAS was conducted to identify spectroscopic signatures of the COF-5 host, guest molecules, and nanoparticles (Fig. 6 and S10–S12 in the ESI†). For example, the C K-edge spectra of COF-5, $\text{Th}(\text{hfa})_4@\text{COF-5}$, and $\text{U}(\text{hfa})_4@\text{COF-5}$ each exhibit a band of closely-spaced features between 284–286 eV that are attributed primarily to the COF-5 host ($\text{C } 1s \rightarrow \text{C}=\text{C } \pi^*$). Additional

features emerged at 286.5 eV in the spectra of $\text{Th}(\text{hfa})_4@\text{COF-5}$ and $\text{U}(\text{hfa})_4@\text{COF-5}$ that are not present for guest-free COF-5, which are attributed to the hfa ligand ($\text{C} 1s \rightarrow \text{C}-\text{O} \pi^*$).¹²⁴ Following decomposition and formation of ThO_2 NPs@COF-5 and UO_2 NPs@COF-5, the high energy features in the C K-edge XAS that are associated with the hfa ligand disappear and the spectra resemble the COF-5 host spectra.

A similar interpretation was applied to the O K-edge XAS data (Fig. 6B). Specifically, COF-5, $\text{Th}(\text{hfa})_4@\text{COF-5}$, and $\text{U}(\text{hfa})_4@\text{COF-5}$ all have O K-edge features at 532 and 535 eV that are attributed primarily to the COF-5 host ($\text{O} 1s \rightarrow \text{C}-\text{C} \pi^* + \text{B}-\text{C} \pi^*$ and $\text{O} 1s \rightarrow \text{C}-\text{C} \pi^* + \text{B}-\text{O} \pi^*$). However, the O K-edge spectra of $\text{Th}(\text{hfa})_4@\text{COF-5}$ and $\text{U}(\text{hfa})_4@\text{COF-5}$ also have a feature at 531.5 eV that is not present for COF-5, which is attributed to the hfa ligand ($\text{O} 1s \rightarrow \text{C}-\text{O} \pi^*$). After decomposition to ThO_2 NPs@COF-5 and UO_2 NPs@COF-5, this low energy feature associated with the hfa ligand also disappeared.

At the F K-edge, intense features that are observed for $\text{Th}(\text{hfa})_4@\text{COF-5}$, $\text{U}(\text{hfa})_4@\text{COF-5}$, and a $\text{Na}(\text{hfa})$ reference are

almost indiscernible in the spectra of ThO_2 NPs@COF-5 and UO_2 NPs@COF-5 (Fig. S12†), which indicates elimination of most fluorinated organic byproducts and retention of trace amounts of fluorine-containing impurities. Actinide $\text{N}_{5,4}$ -edge transitions are also detected for the $\text{Th}(\text{hfa})_4@\text{COF-5}$ and $\text{U}(\text{hfa})_4@\text{COF-5}$ inclusion compounds and for the ThO_2 NPs@COF-5 and UO_2 NPs@COF-5 products (Fig. S12†); however, their exact intensities cannot be quantified due to large background absorptions from B, C, O, and F. Taken together, these results provide confidence that decomposition reactions for the $\text{Th}(\text{hfa})_4@\text{COF-5}$ and $\text{U}(\text{hfa})_4@\text{COF-5}$ inclusion compounds went fully to completion.

Actinide L_3 -edge XANES and EXAFS

The aforementioned results suggest that the synthesis reaction formed nanoparticles according to the designed methodology but do not reveal anything about the atomic-scale structure of the nanoparticles. To this end, An L_3 -edge X-ray absorption fine-

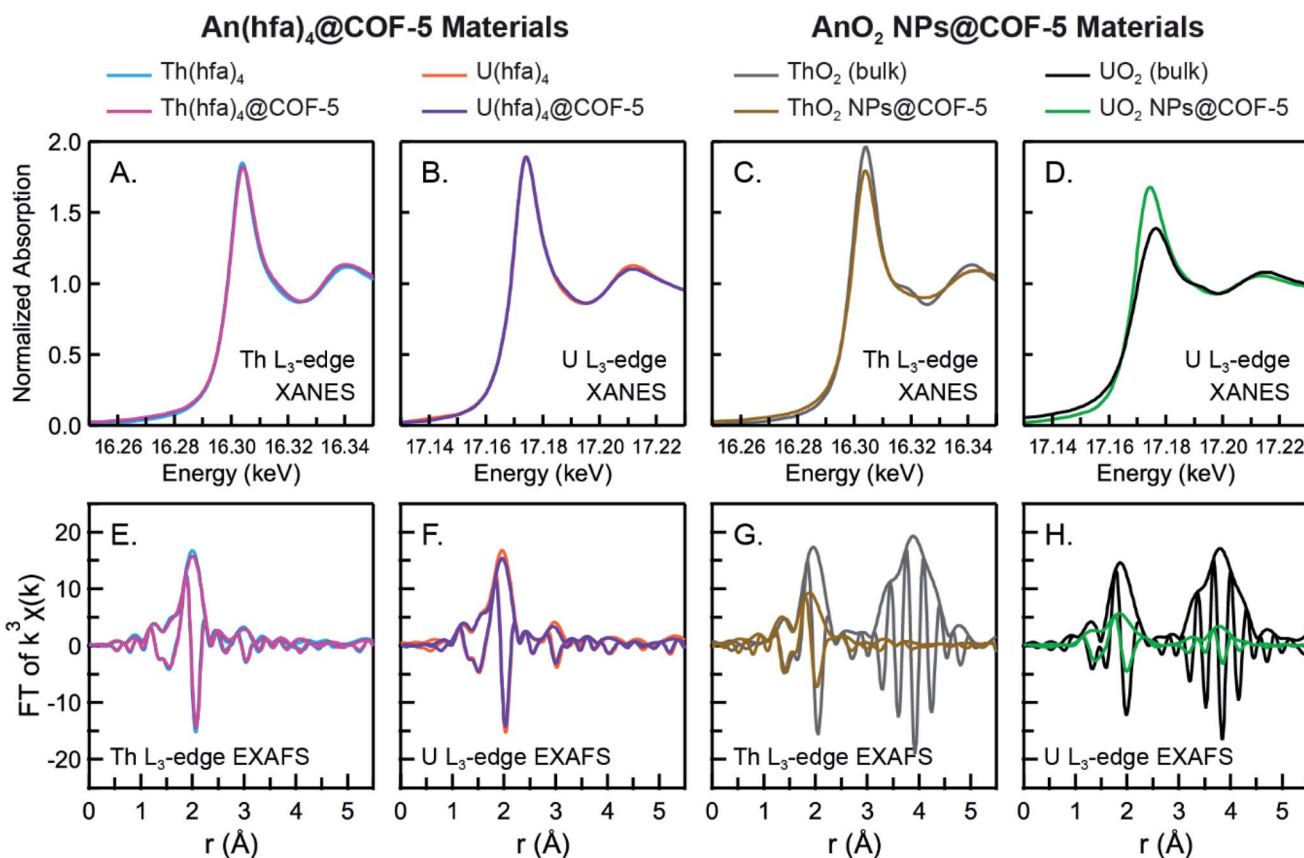


Fig. 7 XAFS L_3 -edge spectra of $\text{Th}(\text{hfa})_4$ and $\text{U}(\text{hfa})_4$ precursors, $\text{Th}(\text{hfa})_4@\text{COF-5}$ and $\text{U}(\text{hfa})_4@\text{COF-5}$ inclusion compounds and ThO_2 NPs@COF-5 and UO_2 NPs@COF-5 compared to bulk ThO_2 and UO_2 counterparts. XANES data are displayed in panels (A)–(D) and the EXAFS FTs in panels (E)–(H) are displayed with both the amplitude (outer envelope) and real component (oscillating component) of the complex transform. EXAFS k^3 weighted data are transformed between 2.5 – 13.5 \AA^{-1} in panels (E) and (F) and between 2.5 – 12.0 \AA^{-1} in panels (G) and (H). Note that r (x axis off the FTs) is different from interatomic distance R due to photoelectron phase shifts. Panels (A) and (B) show the XANES data for pure precursor (teal and orange) and inclusion compounds for Th (magenta) and U (purple) species, respectively. Both XANES and EXAFS FTs (E and F) are nearly identical for the precursors versus inclusion compounds. This reveals that the metal site within the precursor was not affected by its incorporation into COF-5. XANES spectra (C and D) of bulk (gray and black) versus NPs@COF-5 (brown and green) show differences in the white line intensity and a dampening of features. EXAFS spectra (G and H) reveal that the nanoparticles were far more disordered than their bulk counterparts, resulting in a decrease in peak amplitude.



Table 1 Summary of EXAFS-derived fitting parameters. EXAFS parameters of precursors and inclusion compounds

Sample	Path	N^a	R (Å)	σ^2 (Å ²)
U(hfa) ₄	U–O	8	2.382(2)	0.0038(2)
	U–C	10(4)	3.45(2)	0.006(5)
U(hfa) ₄ @COF-5	U–O	9(1)	2.377(8)	0.0042(7)
	U–C	12(4)	3.45(4)	0.010(7)
Th(hfa) ₄	Th–O	9(1)	2.443(6)	0.0037(4)
	Th–C	6(4)	3.45(3)	0.005(9)
Th(hfa) ₄ @COF-5	Th–O	9(1)	2.451(7)	0.0043(5)
	Th–C	4(3)	3.45(2)	0.001(5)

^a S_0^2 values (amplitude reduction factors) set to 1.

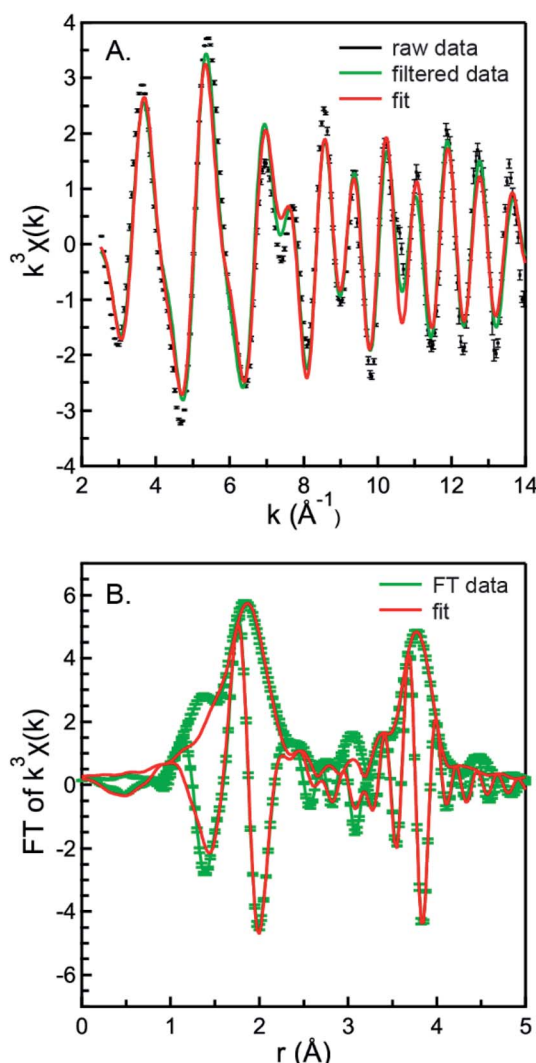


Fig. 8 EXAFS fit results from UO₂ NPs@COF-5. Fitting results compared to data for UO₂ NPs@COF-5 are shown in k -space (top) and r -space (bottom). Fitting results are outlined in Table 2. The fitting range is between 1.4 and 4 Å and the k^3 weighted data are transformed between 2.5–14.0 Å⁻¹. Error bars are included on the raw data, the quality of which is representative of that from other samples in the data set (shown in Fig. S13a–i†).

structure (XAFS) spectroscopy was used to evaluate the local atomic structure (using the extended X-ray absorption fine-structure, or EXAFS, data) and electronic structure (using the X-ray absorption near-edge structure, or XANES, data) of the Th(hfa)₄ and U(hfa)₄ precursors, Th(hfa)₄@COF-5 and U(hfa)₄@COF-5 inclusion compounds, and ThO₂ NPs@COF-5 and UO₂ NPs@COF-5 products.

The first question is whether the Th(hfa)₄ and U(hfa)₄ precursors retained their chemical composition upon formation of the Th(hfa)₄@COF-5 and U(hfa)₄@COF-5 inclusion compounds. Both the XANES (Fig. 7, top-left), and the EXAFS regions of the spectra (Fig. 7E and F) indicate no substantial differences in the electronic or radial structure from the actinide site between the isolated precursor and when it was incorporated into COF-5 for either Th(hfa)₄ or U(hfa)₄. The EXAFS data are displayed as the Fourier transform (FT) of $k^3\chi(k)$, where k is the photoelectron wave vector and the EXAFS function $\chi(k)$ contains the absorption fine-structure oscillations after a suitable background removal.^{125,126} The FT has peaks in the amplitude that correspond to near-neighbor scattering shells, where the position is related to the interatomic distance, R , and the amplitude has information about the number of neighbors (scatterers), N , and the mean-squared displacement of the interatomic-distance distribution, σ^2 , also known as the Debye–Waller factor for the atom pairs (in contrast to the positional Debye–Waller factor in crystallography). It is important to note that the peak positions are shifted a known amount by a phase shift of the photoelectron, and for this and other reasons, detailed fits must be performed to obtain accurate metrical information. For all the fits reported here, the first two nearest-neighbor scattering shells were included, starting with an An–O shell. In the case of the precursors, the second shell was an An–C shell. Derived EXAFS fitting parameters for the free precursors and when incorporated into COF-5 (Table 1) are in excellent agreement (the same within error), indicating that the precursors existed in their nominal form within COF-5. A representative fit and data set are shown in Fig. 8 and all other fits compared to bulk data are shown in Fig. S13a–i (see ESI for further details†).

In contrast, substantial differences are observed in the XANES and EXAFS data between the ensuing nanoparticles and their bulk counterparts (Fig. 7, right and Table 2). To begin, the edge positions and ThO₂ white line position are similar for

Table 2 EXAFS parameters of AnO₂ NPs@COF-5 versus bulk AnO₂

Sample	Path	N^a	R (Å)	σ^2 (Å ²)
UO ₂ (bulk)	U–O	8(1)	2.34(3)	0.005(1)
	U–U	12(2)	3.87(1)	0.0013(6)
UO ₂ NPs@COF-5	U–O	6(1)	2.34(1)	0.011(1)
	U–U	3(1)	3.860(8)	0.004(1)
ThO ₂ (bulk)	Th–O	9(1)	2.424(7)	0.0026(5)
	Th–Th	13(4)	3.948(5)	0.0005(4)
ThO ₂ NPs@COF-5	Th–O	7(1)	2.38(1)	0.008(1)
	Th–Th	2(2)	3.891 ^b	0.005(5)

^a S_0^2 values (amplitude reduction factors) set to 1. ^b Value frozen during fit.



ThO_2 NPs@COF-5 and bulk ThO_2 , which is consistent with no substantial change in the Th valence state. However, the white line position in the UO_2 NPs@COF-5 is shifted to lower energy by 2 eV from the bulk UO_2 position. As described in greater detail in the discussion of the EXAFS results below, this shift is not accompanied by a lengthening or shortening of the U–O or U–U interatomic distances (Table 2) which might have been indicative of a deviation from the tetravalent oxidation state in UO_2 NPs@COF-5. Alternative explanations for the white line shift include greater localization of the 5f electrons in UO_2 NPs@COF-5 or increased charge transfer from the O 2p orbitals in UO_2 NPs@COF-5 relative to bulk UO_2 .¹²⁷ The uranium L_3 -edge XANES also exhibit a more intense white line for the UO_2 NPs@COF-5 *versus* bulk spectra, which is consistent with the anticipated trend for small nanoparticles whereby a sharpening of the 5d band is driven by the loss of long-range order.¹²⁸ The opposite trend, however, is observed for the ThO_2 NPs@COF-5 compared to bulk ThO_2 . This has been observed previously for sub-10 nm ThO_2 particles^{129,130} and can be attributed to differences in the occupied states between the two actinides, given that electronic structure and size confinement often are competing effects in nanoparticle XANES.¹³¹ Differences are also observed between the particles investigated in this study and 3 nm PuO_2 colloids reported previously, where the white line is decreased in energy compared with bulk as we observe for UO_2 , but lowered in intensity compared to bulk, similar to the ThO_2 case.⁷⁵ In both ThO_2 and UO_2 NPs@COF-5 cases, the first post-edge feature is missing, which has previously been observed for 2.5 nm ThO_2 NPs and attributed to a lowering in the number of coordinating atoms.¹³² The origin and universality of these differences in L_3 -edge XANES spectra for actinide nanoparticle systems relative to their bulk analogs is the subject of ongoing investigation. Further in-depth study will be required to elucidate actinide-specific trends in electronic structure, as well as how differences are affected by size, shape, and surface chemistry, all of which have been suggested to play a role in the electronic structure of actinide oxide nanoparticles.^{72,75,130,132} Specifically, the dependence of these parameters on nanoparticle magnetic susceptibility, which is intimately connected to electronic properties, will be described in detail in a future manuscript.

The EXAFS data provide a more precise result. The Fourier transforms (FTs) in Fig. 7G and H show that the An–O scattering shell of the nanoparticles appear to directly correspond with their bulk counterparts; however, both the first (An–O) and the second (An–An) scattering shells are far diminished in their intensities. Fitting the first (Th–O and U–O) and second (Th–Th and U–U) coordination shells reveals interatomic distances for the AnO_2 NPs@COF-5 materials that are the same, on average, as those observed in their bulk analogs. No evidence for An–B or An–C bonds was obtained within the detection limits of EXAFS and because results from PXRD, XAS and IR spectroscopy showed no decomposition of the COF-5 template, the possibility that complex oxides containing significant amounts of boron or carbon were formed was ruled out. For the case of the ThO_2 NPs@COF-5, the second shell (Th–Th) was not clearly visible,

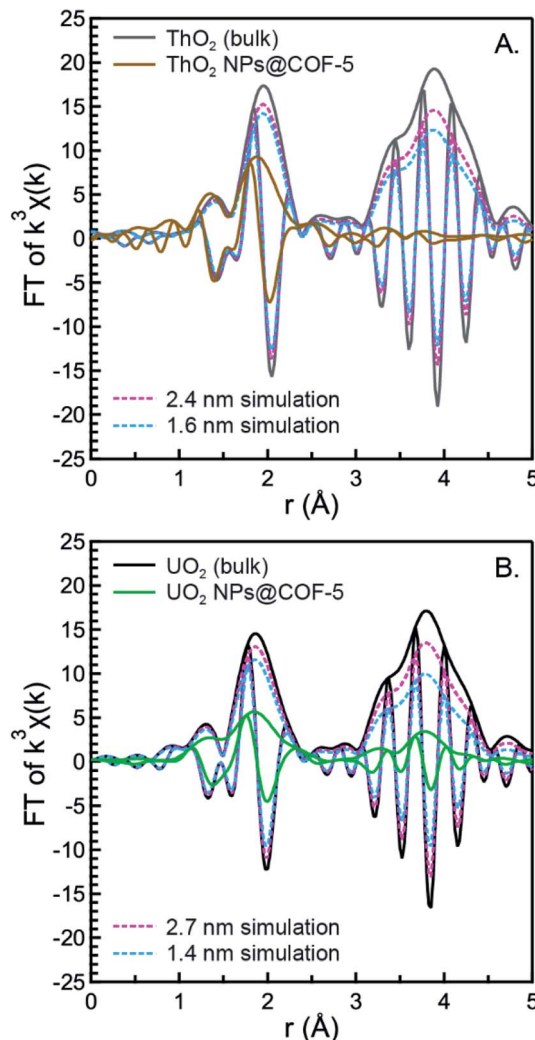


Fig. 9 Simulations using the Calvin method compared to (A) ThO_2 NPs@COF-5 and (B) UO_2 NPs@COF-5 using TEM-determined (pink, dotted) and SAXS-determined (light-blue, dotted) nanoparticle sizes.

although fitting results suggest that there could be up to 4 Th neighbors if coupled with a large σ^2 parameter.

The reduction of the FT peak amplitudes may be due to increased disorder, a particle-size effect, or both. To determine which is the cause of the amplitude reduction, spectra for the AnO_2 NPs@COF-5 materials were compared with simulated spectra for nanoparticles of the same size using the method

Table 3 Analysis using an Einstein model of precursor, inclusion compound and NPs@COF-5

Structure	Static disorder (\AA^2)	Einstein T (K)
$\text{Th}(\text{hfa})_4$	-0.00083 ± 0.00008	380 ± 3
$\text{Th}(\text{hfa})_4@\text{COF-5}$	0.00014 ± 0.0004	372 ± 4
ThO_2 NPs@COF-5	0.004 ± 0.0007	464 ± 56
$\text{U}(\text{hfa})_4$	-0.0005 ± 0.0003	369 ± 6
$\text{U}(\text{hfa})_4@\text{COF-5}$	0.001 ± 0.0005	361 ± 18
UO_2 NPs@COF-5	0.007 ± 0.001	400 ± 59



developed by Calvin *et al.*,¹³³ which models decreases in peak intensity based on changes in average coordination number with decreased particle size. The results of this analysis (Fig. 9, S15 and S16†) show that the decrease in FT peak amplitudes cannot be modeled by a decrease in coordination number alone. Therefore, the decrease in peak amplitudes is also caused by larger σ^2 parameters for the AnO_2 NPs@COF-5 relative to bulk ThO_2 and UO_2 .

Thermal (σ_{th}^2) and static (σ_s^2) contributions to σ^2 ($\sigma^2 = \sigma_{\text{th}}^2 + \sigma_s^2$) were investigated for $\text{Th}(\text{hfa})_4$, $\text{U}(\text{hfa})_4$, $\text{Th}(\text{hfa})_4@\text{COF-5}$, $\text{U}(\text{hfa})_4@\text{COF-5}$, ThO_2 NPs@COF-5 and UO_2 NPs@COF-5 by applying an Einstein model^{134,135} to the fit results from the first coordination shell (Th–O or U–O) as a function of temperature, from cryogenic (50 K) to room temperature (300 K) (Table 3 and ESI†). This fitting process¹³⁶ was used to determine whether decreases in FT peak amplitude resulted from a larger, static distribution of distances within the precursors of the NPs@COF-5. Static disorder values are negligible for both $\text{Th}(\text{hfa})_4$ and $\text{Th}(\text{hfa})_4@\text{COF-5}$, which indicates that the structure of the $\text{Th}(\text{hfa})_4$ molecule was not perturbed following incorporation into the COF-5 host. The same is true for $\text{U}(\text{hfa})_4$, although a slight increase in the static structural disorder is observed for $\text{U}(\text{hfa})_4@\text{COF-5}$ that is only significant to 2-standard deviations. Overall, these negligible-to-very small structural disorders show that the precursor was not strained structurally when incorporated into COF-5, and that the σ^2 component was caused primarily by thermal vibrations.

More significant static disorder values of $\sigma_s^2 = +0.004 \text{ \AA}^2$ and $+0.007 \text{ \AA}^2$ are observed in the first shell for ThO_2 NPs@COF-5 and UO_2 NPs@COF-5, respectively, both of which are substantially larger than the total σ^2 observed in bulk ThO_2 and UO_2 . Such an increase in static disorder likely results from the larger distribution of An–O bond distances in nanoparticle surface layers. Regardless of whether TEM or SAXS is used to determine nanoparticle size, a significant number of the actinide metal atoms are estimated to be at the surface. In the case of UO_2 NPs@COF-5, at least 30% of the uranium atoms are at the surface based on the upper size limit provided by TEM (2.7 nm) while upwards of 60% are at the surface based on the average size provided from SAXS (1.4 nm).

Given the high percentage of surface atoms in the ThO_2 NPs@COF-5 and UO_2 NPs@COF-5, the EXAFS spectra were also scrutinized for peaks that might provide evidence of interactions between the nanoparticles and the COF-5 host or other organic residues. For tetravalent actinide oxo hydroxide molecular clusters, peaks at lower r values have been previously observed in the L_3 -edge EXAFS that were attributed to shorter An–O bonds involving organic ligand species.¹³⁷ In contrast, no peaks are observed in the spectra of ThO_2 NPs@COF-5 and UO_2 NPs@COF-5 that are not also present in the spectra for bulk ThO_2 and UO_2 . Specifically, the lower r peaks observed below 1.5 Å in r -space for both the ThO_2 NPs@COF-5 and UO_2 NPs@COF-5 are of comparable intensity to those observed in bulk ThO_2 and UO_2 (Fig. 7G and H), indicating that these features are the result of artifacts in the background.^{138–141} The spectra are most effectively modeled using bulk pathways alone. The lack of such a contribution suggests that the ThO_2 and UO_2 NPs were not

strongly bound to the COF-5 host, and that any interactions must have been weak (e.g., van der Waals) and/or with low coverage. Taken together with the XANES and EXAFS results described above, these results show that ThO_2 and UO_2 nanoparticles prepared in the COF-5 template were not passivated with strong binding surface ligands and best regarded as compositional and crystallographic nanoscale analogs of bulk ThO_2 and UO_2 .

Discussion

The multi-pronged characterization effort, including the imaging, diffraction and spectroscopic approaches described above was necessary to fully characterize the structural properties of the complex multi-component nanoparticle systems. Combined, the techniques provide atomic- to micron-scale probes, element and bulk-level specificity, and measurements that are locally and globally significant. For example, PXRD, IR spectra, C and O K-edge XAS, and L_3 -edge XANES and EXAFS data all show that the structure and composition of both precursors, $\text{Th}(\text{hfa})_4$ and $\text{U}(\text{hfa})_4$, is retained upon formation of the inclusion compounds, $\text{Th}(\text{hfa})_4@\text{COF-5}$ and $\text{U}(\text{hfa})_4@\text{COF-5}$, respectively. The COF-5 template material was also examined at each step of the synthetic process, with IR spectra and C and O K-edge XAS showing that its composition remained unchanged and PXRD, SAXS, TEM and STXM showing that its crystalline structure and morphology was not perturbed.

A critical question is whether the COF-5 host directed nanoparticle formation, and thereby functioned effectively as a template. Several of the measurements support this hypothesis. First, following sublimation of the precursors into the COF-5 material, the mass increased by 40–60% which is consistent with predictions based on the COF-5 pore volume and precursor crystallographic densities. STXM elemental mapping shows that U and Th was distributed uniformly throughout the organic matrix, and PXRD shows an inversion of the lower-order reflections as expected for incorporation of molecules within host pores.¹⁰⁵ These results suggest that the molecular precursors are guests within the COF-5 host, and not simply mixed or co-crystallized with larger COF-5 particles. Similar results observed by TEM and STXM imaging for the ThO_2 and UO_2 nanoparticles show that the nanoparticles were embedded within the COF-5 material and have not migrated to the surface of the COF particles, as has been observed in other cases.¹⁰⁸ Most importantly, the average nanoparticle diameters derived from TEM and SAXS are below 3 nm, which suggests that nanoparticle growth is directed by the COF-5 structure, which has 2.7 nm diameter pores.⁹⁹ As shown in Fig. 3C, the calculated Schulz distribution of particle sizes based on the average diameter and polydispersities determined from SAXS is bounded nicely by the diameter of the COF-5 pores. No significant differences between ThO_2 and UO_2 nanoparticle sizes are found when accounting for the polydispersities, which suggests that the nanoparticle size is controlled primarily by the COF template. This finding contrasts with observations from colloidal syntheses, where similar conditions used to form UO_2



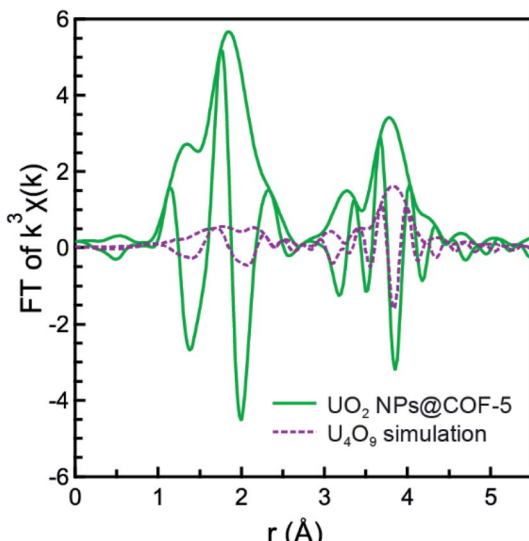


Fig. 10 EXAFS experimental spectrum of UO_2 NPs@COF-5 (green) compared to a FEFF simulation of U_4O_9 (purple, dotted).

and ThO_2 nanoparticles resulted in particles of varying sizes and morphologies.^{72,76}

The atomic scale structure and composition of the ThO_2 NPs@COF-5 and UO_2 NPs@COF-5 are compared directly to their bulk counterparts using L_3 -edge XAFS. This analysis considers how having a high percentage of surface atoms might alter the nanoparticle structure, particularly within particle surface layers. The contribution to the XAFS signal is the same for each absorbing atom in the beam path. Therefore, XAFS is equally sensitive to atoms within the nanoparticle core and to atoms in other coordinating environments that may be unique to nanoparticle surface layers. Despite the high percentage of surface atoms, fitting the EXAFS regions for ThO_2 NPs@COF-5 and UO_2 NPs@COF-5 (Fig. 8 and S13h†) was best achieved using bulk ThO_2 and UO_2 pathways, respectively. This model was foreseeable for ThO_2 , which was unlikely to form sub- or hyper-stoichiometric oxides.¹⁴² However, finely-divided UO_2 powders are known to oxidize readily to U_4O_9 at surfaces and along grain boundaries,¹⁴³ and previous UO_2 nanoparticle synthesis reactions have provided evidence for the formation of secondary super-stoichiometric UO_{2+x} phases.¹⁴⁴ Similarities between the L_3 -edge spectra of ThO_2 NPs@COF-5 and UO_2 NPs@COF-5 and bulk ThO_2 and UO_2 counterparts provide initial support for the UO_2 formulation. In addition, the L_3 -edge spectrum for UO_2 NPs@COF-5 does not match those reported previously for a range of UO_{2+x} species.¹⁴⁵ To further consider possible formation of a higher oxide, a variety of U_xO_y structures were simulated using FEFF calculations. Fig. 10 compares a representative simulation for U_4O_9 , the first binary uranium oxide with a higher oxygen stoichiometry than UO_2 ,¹⁴⁶ compared with the experimental spectrum for UO_2 NPs@COF-5 (see the ESI† for additional simulations). The comparison in Fig. 10 exemplifies a key attribute of all the simulated spectra that is absent in the experimental data for UO_2 NPs@COF-5: the first shell intensity is almost entirely diminished for U_4O_9 ,

indicating the presence of distortions that would manifest as higher static disorder in the single pathway model used for fitting the UO_2 NPs@COF-5 data. As shown in Table S9,† the static distribution in U–O bond lengths expected for any perfectly crystalline higher oxide incorporation is higher than that extracted from an Einstein fitting model (0.031 \AA^2 for U_4O_9 vs. 0.007 \AA^2 in the UO_2 NPs@COF-5). The increased bond length distribution but overall similarity in average structure to UO_2 is in line not only with our ThO_2 results, where a super-stoichiometric oxide would not be expected, but also with previous nanoscale systems where the AnO_2 formulation was assigned.^{53,130,147,148} Neither the XANES nor the EXAFS regions (Fig. 10 and S17–S19†) match the data trends better than UO_2 , nor do they provide evidence of shorter U–O bonds that are characteristic of UO_{2+x} .^{145,149} This analysis suggests that, as with ThO_2 NPs@COF-5, UO_2 is the most representative chemical formulation for the UO_2 NPs@COF-5, both in the nanoparticle interior and at the surface.

Because colloidal nanocrystal and nanocluster syntheses typically require strong-binding ligands for surface stabilization,¹⁵⁰ we considered whether strong binding surface species stabilized the ThO_2 NPs@COF-5 or UO_2 NPs@COF-5 materials. Previous studies show that the presence of strong binding ligands often leads to oxidation of surface layers for colloidally synthesized nanoparticles. Specifically, XANES spectra for sub 5 nm nanoparticles have shown significant differences in average oxidation state that reflect the changes these strong-binding ligands induced on the nanoparticle surface.^{78,79} In the EXAFS region, studies on both nanoparticles¹⁵¹ and clusters¹³⁷ show low-*r* peaks at different distances than those expected in the first-coordination sphere of bulk analogs that are indicative of surface-ligand bonds. In the present study, the L_3 -edge XANES of ThO_2 NPs@COF-5 and UO_2 NPs@COF-5 only show signatures of the Th^{4+} and U^{4+} atoms observed in bulk ThO_2 and UO_2 and no shift that can be attributed to higher oxides. In addition, no low-*r* peaks are observed in the L_3 -edge EXAFS for ThO_2 NPs@COF-5 or UO_2 NPs@COF-5 that are not also present in bulk as background artifacts and the presence of strong-binding surface ligands can be ruled out. The lack of strong-binding surface ligands is increasingly significant for ultra-small nanoparticles, given that evidence has shown increasing ligand packing densities with decreasing particle size.¹⁵² The aforementioned results, however, suggest that our nanoparticles were not passivated by strong-binding surface ligands and therefore constitute a suitable system to investigate actinide structure as a function of grain size. Namely, the structural properties of surface and interior atoms outlined herein are applicable to understanding the effects of decreased grain size in extended solids, such as those important for the development of advanced nuclear fuels.

While the L_3 -edge EXAFS results show that the composition of the ThO_2 and UO_2 nanoparticles resembled their bulk analogs without contributions from strong-binding surface ligands, they also reveal subtle but important distinctions in their crystallographic structures. For example, Fig. 7 shows that the EXAFS peak intensities for ThO_2 NPs@COF-5 and UO_2 NPs@COF-5 are reduced compared to bulk ThO_2 and UO_2 ,



respectively. In particular, the second shell intensities are reduced more than the first shell, as expected in nanoparticles due to the finite size of such systems. Simulations were performed to illustrate the effect of reductions in coordination number on the EXAFS spectra for ThO_2 NPs@COF-5 and UO_2 NPs@COF-5 by applying a scaling factor to the bulk data as a function of R consistent with a given particle size,¹⁵³ which we refer to as the Calvin method.¹⁵⁴ (Fig. 9, S15 and S16 in the ESI†). In both cases, decreases in peak intensity are predicted by these simulations as particle size is systematically reduced from bulk. Notably, the decreases in peak intensity predicted by the Calvin method are less drastic than those observed experimentally, since this approach assumes all intensity reductions are due to changes in coordination number and does not account for differences in static disorder. Larger static disorder values for the NPs@COF-5 samples compared to bulk are confirmed from fitting to an Einstein model, and indicate a larger distribution of interatomic distances present in the nanoparticles (see Table 3 and ESI† for additional details). It should be noted that the static disorder was slightly decreased through the post-synthesis annealing step in H_2 at 300 °C, which increased nanoparticle crystallinity (see Fig. S21†). Still, the nanoparticles remain significantly disordered, on average, compared with bulk analogs. Taken together, these techniques show that the overall nanoparticle structure resembles a disordered form of the bulk, such that both the long- and short-range order was disrupted, likely as a result of structural distortions at the surface as described below.

The results discussed above also shed light onto the structure of surface layers within the nanoparticles. Because the surfaces are a major component of the overall UO_2 NPs@COF-5 structure (with ~60% of U atoms being surface atoms based on average size estimates from SAXS), if the nanoparticle surface layers were oxidized to a higher oxide, then the higher oxide structure would comprise a majority of the EXAFS signature. By this logic, because the L_3 -edge EXAFS of UO_2 NPs@COF-5 shows no evidence of higher oxide formation, the possibility of a higher oxide that is only present on the nanoparticle surfaces can be ruled out. EXAFS cannot explicitly rule out scenarios where a submonolayer of higher oxide or other minor impurities are present, or the possibility of slightly superstoichiometric oxides,¹⁴⁵ which would be outside the detection limit of our measurements. However, previous work using Sessile drop and grain boundary grooving experiments suggest that a sub-monolayer of higher oxide would be unlikely to form, showing that deviations in surface stoichiometry from that of UO_2 result in increased surface and interfacial energies, making it energetically unfavorable to have a sub-monolayer of higher oxide.¹⁵⁵ In contrast, surface atoms in the lower energy (111) and (110) surface facets expected for quasi-spherical UO_2 particles have the means to adjust from their expected bulk positions to lower surface energy considerably. For example, on (111) surface facets, a contraction of the outer oxygen sphere can help stabilize dangling uranium surface bonds.^{156,157} These surface layer reconstructions may play a role in the high degree of static disorder observed in Th–O and U–O bonds within the nanoparticles by helping to stabilize the nanoparticle surface without necessitating the formation of a higher oxide. Such a trend

is well-aligned with what has previously been observed in U_{38} clusters, where interior atoms of the particle are more well-ordered than the surface layers, which exhibit a greater degree of rearrangement from bulk-like UO_2 .⁵⁷ The L_3 -edge EXAFS of ThO_2 NPs@COF-5 and UO_2 NPs@COF-5 both show a decrease in coordination number which may be indicative of the formation of μ -2 or μ -3 bridging oxos as a possible surface stabilization method, as has been observed previously in single-crystal XRD investigations of uranium(IV) molecular clusters.^{65,158} If multiple monodentate hydroxide groups were instead stabilizing the surface, a decrease in coordination number would not be expected, making bridging oxos or an oxo-hydroxide combination a more plausible option. This could help explain, along with other surface relaxation effects, the increased disorder observed. However, if either oxo or hydroxide groups were present, they had comparable An–O distances to those in UO_2 and ThO_2 , since the average interatomic distances extracted from EXAFS matched the bulk case.

Surface layer distortions are known to have significant consequences for the properties of transition metal nanoparticles,^{159–163} and may have important implications on the ability of actinide oxide based nuclear fuels to withstand self-radiative damage. The implications of disordered surface structure on radiation damage are twofold. First, surface defects enable safer release for fission products without disturbing internal structure⁵ by providing a mechanism for defect escape at the particle surfaces.^{164,165} This is in line with studies that show initial grain boundaries in polycrystalline nuclear fuels remained intact in spite of high burnup structure formation.¹⁶⁶ Second, fuel swelling is typically caused through amorphization processes, leading to failure.^{167,168} This amorphization damage and related swelling can be mitigated by starting with an amorphous material.¹⁶⁹ The disordered nanoparticle surface layers discovered through this study therefore provide insight into these two mechanisms through which radiation damage can be minimized by incorporating nanostructured UO_2 in advanced nuclear fuels.

Conclusion

The results presented here show that ultra-small ThO_2 and UO_2 nanoparticles can be prepared free from strong surface-binding ligands by using COF-5 as a rigid template, making them ideal analogs to systematically study the effects of decreased grain size within extended solids. The synthetic process began by subliming $\text{Th}(\text{hfa})_4$ and $\text{U}(\text{hfa})_4$ precursors into the pores of COF-5 under vacuum, resulting in composite materials that preserved the original structure and composition of the guest precursor molecules and COF-5 host. The precursors decomposed selectively upon heating $\text{Th}(\text{hfa})_4$ @COF-5 and $\text{U}(\text{hfa})_4$ @COF-5 in the presence of H_2O vapor and formed ThO_2 and UO_2 nanoparticles. Analysis using PXRD, TEM, and SAXS confirms that the nanoparticles were ultra-small (sub-3 nm) and that their growth was confined by the pores of the COF-5 template (2.7 nm).⁹⁹ Further characterization using IR spectroscopy and soft X-ray spectromicroscopy at the C, O, and F K-edges as well as the Th or U N_{5,4}-edges shows that the two-step synthetic process resulted in complete formation of the ThO_2 NPs@COF-5 and UO_2



NPs@COF-5 products without detectable decomposition of the COF-5 template or strong host-guest interactions.

To thoroughly understand the structural properties of the composite, three-dimensional products, an in-depth study using Th and U L₃-edge XANES and EXAFS was employed to determine structure and composition at the surface and in the core of both the ThO₂ and UO₂ nanoparticles. Fitting to the EXAFS regions for ThO₂ NPs@COF-5 and UO₂ NPs@COF-5 was best achieved using bulk ThO₂ and UO₂ pathways alone. No plausible fits could be derived that would support identification of secondary superstoichiometric UO_{2+x} or other higher oxide phases at the surface of the UO₂ nanoparticles. Analysis of the experimental spectra using an Einstein vibrational model to extract estimates of static disorder in conjunction with FEFF simulations and Calvin analysis show that the ThO₂ and UO₂ nanoparticle structures feature a larger distribution of bond lengths indicative of distorted surface layers.

The template-directed synthesis approach described herein is uniquely advantageous because, despite their exceptionally small size, the nanoparticle surfaces remained free from strong-binding organic ligands that could complicate analyses of their physical properties and comparisons to bulk material. As such, they presented an opportunity to trace the origins of nanoscale chemical phenomena from more well-understood bulk actinide behavior through structural comparisons, which are intimately connected to their properties. This synthetic methodology is also ideal for exploring the nanoscale chemistry of transuranic elements given the minimal amount of metal required compared to conventional colloidal nanoparticle syntheses, which is desirable given the high radioactivity and requirements for waste-minimization, recovery and reuse of these elements. Along these lines, future work will explore how 5f-electron behavior varies as a function of (1) nanoparticle size by varying the template, and (2) 5f-orbital energies by incorporating Np(hfa)₄ and Pu(hfa)₄ precursors.

Experimental

General considerations

All reactions were performed using standard Schlenk-line techniques or in an MBraun dry box (<1 ppm O₂/H₂O) unless noted otherwise. All glassware was dried at 150 °C for at least 12 hours, or flame dried under vacuum prior to use. Toluene, *n*-pentane, *n*-hexane and diethyl ether were degassed by passing through an argon flow, passed through a column of activated alumina, stored over 4 Å molecular sieves and vacuum transferred immediately prior to use. Tetrahydrofuran was vacuum transferred from Na/benzophenone. Benzene-*d*₆ (Cambridge Isotope Laboratories) was distilled from sodium benzophenone and degassed by three freeze-pump-thaw cycles. Hexafluoroacetylacetone was distilled, placed over 4 Å molecular sieves, and stored under argon. The 2,3,5,7,10,11-hexahydroxytriphenylene used to prepare COF-5 was purified by Soxhlet extraction with H₂O under argon prior to use. COF-5 was prepared by a literature procedure, activated at 100 °C and 10⁻⁵ torr for 24 h, and characterized by PXRD and IR spectroscopy prior to use.¹⁷⁰ Th(O-2,6^tBu₂C₆H₃)₄ was prepared according to the literature procedure.¹⁷¹ Ultrapure UO₂ was

prepared according to the published procedure¹⁷² by conversion of uranyl peroxide to UO₃ in air at 400 °C for 18 h, followed by reduction with H₂ at 600 °C, and characterized by PXRD, SQUID magnetometry, and L₃-edge XAFS. All other reagents were acquired from commercial sources and used as received. NMR spectra were recorded at ambient temperature (unless otherwise indicated) on a Bruker Avance DPX 300 MHz Ultrashield NMR spectrometer and referenced internally using the residual protio solvent resonances relative to tetramethylsilane (δ 0) for ¹H and ¹³C{¹H} data, and hexafluorobenzene (δ -164.9) relative to trichlorofluoromethane (δ 0) for ¹⁹F{¹H} data. IR samples were prepared as Nujol mulls between KBr round cell windows and the spectra were recorded on a Mattson Sirius 100 FT-IR spectrometer. Melting points were determined using sealed capillaries prepared under Ar and are uncorrected. Elemental analyses were determined at the Microanalytical Facility of the College of Chemistry, University of California, Berkeley.

Synthesis of Th(hfa)₄

Th(O-2,6^tBu₂C₆H₃)₄ (0.532 g, 0.505 mmol) was dissolved in Et₂O (~20 mL) in a 100 mL Schlenk flask. Hexafluoroacetylacetone (0.30 mL, 2.1 mmol) was added *via* syringe to a 50 mL Schlenk flask with Et₂O (~20 mL). The solution of Th(O-2,6^tBu₂C₆H₃)₄ was chilled to -78 °C, and then the solution of hexafluoroacetylacetone was added slowly over ~10 min period. No immediate color change was observed, and the solution was allowed to warm to room temperature. After stirring for ~15 min, the solution had turned pale yellow, and was then filtered into a 50 mL Schlenk tube and concentrated to ~10 mL. Off-white crystals of Th(hfa)₄ were then formed after chilling the solution to -20 °C for 12 h. The mother liquor was decanted and the compound was recrystallized to yield colorless crystals which were then dried *in vacuo* to yield Th(hfa)₄ as a white powder (0.431 g, 81%). ¹H NMR (benzene-*d*₆, 300 MHz): δ_H 6.03 (s, 4H, CH), 2.81 (s, 2H, H₂O). ¹³C{¹H} NMR (benzene-*d*₆, 75 MHz): δ_C 95.4 (s, CH), 117.8 (q, CF₃, J_{C-F} = 284 Hz), 179.1 (q, CO, J_{C-F} = 37 Hz). ¹⁹F{¹H} NMR (benzene-*d*₆, 282 MHz): δ_F -78.9 (s, CF₃). IR (KBr-Nujol): 1648 (m), 1622 (sh), 1567 (w), 1541 (w), 1260 (m), 1214 (sh), 1145 (m), 1103 (w), 810 (m), 770 (w), 742 (sh), 656 (m), 587 (m). Anal. calcd for Th(hfa)₄ - C₂₀H₄F₂₄O₈Th (1060.26): C, 22.65; H, 0.38. Found: C, 22.35; H, 0.37. Intractable twinning problems were encountered during multiple attempts at structural determination using single-crystal X-ray diffraction with carefully-grown crystals of Th(hfa)₄. Alternatively, crystals suitable for X-ray diffraction were obtained by slow evaporation of a concentrated solution of Th(hfa)₄ in a 1 : 1 mixture of DME/hexane, which provided the structure of the dimethoxyethane (dme) adduct, Th(hfa)₄(dme). Structural features are discussed in the ESI.†

Synthesis of U(hfa)₄

The literature procedure was followed.¹¹² Purification was effected by cooling at -35 °C a Et₂O solution over 24 h, which afforded the product as tan crystals following filtration. ¹H NMR (benzene-*d*₆, 300 MHz): δ_H 12.74 (s, 4H, CH). ¹H NMR (acetone-*d*₆): δ_H 12.65 (s, 4H, CH). ¹H NMR (acetonitrile-*d*₃): δ_H 12.61 (s, 4H, CH). ¹³C{¹H} NMR (benzene-*d*₆, 75 MHz): δ_C



134.10 (s, CH), 143.5 (q, CO, $J_{C-F} = 39$ Hz), 164.6 (q, $J_{C-F} = 283$ Hz, CF₃). ¹⁹F{¹H} NMR (benzene-*d*₆, 282 MHz): δ –80.9 (s, CF₃). IR (KBr-Nujol): 1646 (m), 1620 (m), 1570 (w) and 1542 (w) (ν (C=O or C=C) – Lit: 1538, 1560, 1620, 1642 cm⁻¹ and 1538, 1568, 1619 and 1643 cm⁻¹), 1306 (sh), 1258 (m), 1233 (br), 1212 (br), 1150 (m), 1101 (w), 811 (m), 769 (w), 746 (m), 737 (m), 660 (m), 587 (m). Mp 96–99 °C (Lit: 90 °C). Crystals suitable for X-ray diffraction were obtained by sublimation at room temperature and 7×10^{-5} torr. Structural features are discussed in the ESI.†

Synthesis of Th(hfa)₄@COF-5

A vial containing activated COF-5 (33.2 mg) was placed upright in a Schlenk flask alongside a separate vial containing an excess of Th(hfa)₄ (100.3 mg). While bulk amounts were synthesized in order to be used for multiple characterization techniques, it should be noted that the synthesis has proven successful with as low as 1 mg of starting material. After reducing the pressure to 4×10^{-5} torr, the system was sealed under static vacuum and stored at room temperature for 48 h. During this time the off-white COF-5 powder darkened and the volume of Th(hfa)₄ visibly decreased. The product was isolated as a beige powder (91.8 mg, 64 wt% Th(hfa)₄). IR (cm⁻¹): 1646 (br) 1523 (s), 1493 (s), 1396 (m), 1349 (s), 1322 (s), 1241 (s), 1211 (sh), 1159 (s), 1103 (w), 1078 (s), 1021 (s), 974 (m), 848 (s), 834 (s), 730 (m), 673 (sh), 657 (s), 615 (m).

Synthesis of U(hfa)₄@COF-5

A vial containing activated COF-5 (31.4 mg) was placed upright in a Schlenk flask alongside a separate vial containing an excess of U(hfa)₄ (79.4 mg). As with Th(hfa)₄@COF-5, bulk synthesis amounts were needed for subsequent characterization. After reducing the pressure to 4×10^{-5} torr, the system was sealed under static vacuum and stored at room temperature for 48 h. During this time the off-white COF-5 powder darkened and the volume of U(hfa)₄ visibly decreased. The product was isolated as a tan powder (84.1 mg, 63 wt% U(hfa)₄). IR (cm⁻¹): 1667 (sh), 1646 (m), 1621 (w), 1564 (w), 1540 (sh), 1524 (w), 1492 (m), 1325 (m), 1259 (m), 1242 (m), 1216 (m), 1158 (m), 1105 (w), 1076 (m), 1021 (m), 975 (w), 892 (w), 848 (m), 833 (m), 811 (w), 768 (w), 746 (m), 658 (m), 612 (w), 588 (m).

Removal of COF-5 guests

In a representative example, suspending U(hfa)₄@COF-5 in Et₂O immediately resulted in formation of an off-white powder and brown liquid. The liquid was decanted, and the solids were washed again with Et₂O. After drying, the residual solids were identified as COF-5 based on IR spectroscopy and powder XRD. Applying a dynamic vacuum of 1.5×10^{-5} torr to U(hfa)₄@COF-5 and heating above 100 °C for more than 48 h also resulted in guest removal.

Synthesis of ThO₂ NPs@COF-5

A vial containing Th(hfa)₄@COF-5 (58 mg) was heated in a Schlenk flask at 200 °C for 3 d under a flow of Ar that was

passed through a bubbler of H₂O at a rate of approximately 60 cm³ min⁻¹. After drying *in vacuo* (6×10^{-5} torr) at 150 °C for 5 h, the resulting solid was annealed at 300 °C under a flow of pure H₂ to improve crystallinity. The product was obtained as a dark gray powder (35.2 mg), which was handled with rigorous exclusion of oxygen and moisture during all subsequent analyses. IR (cm⁻¹): 1691 (br), 1624 (br), 1523 (m), 1492 (s), 1395 (sh), 1350 (s), 1325 (s), 1240 (s), 1207 (sh), 1162 (m), 1077 (m), 1020 (m), 973 (w), 849 (m), 834 (m), 673 (sh), 657 (m), 614 (m).

Synthesis of UO₂ NPs@COF-5

The reaction proceeded exactly as described above for ThO₂ NPs@COF-5. Beginning with U(hfa)₄@COF-5 (51.4 mg), the product was obtained as a dark gray powder (32.4 mg). IR (cm⁻¹): 1691 (br), 1624 (br), 1523 (m), 1492 (s), 1395 (sh), 1350 (s), 1325 (s), 1240 (s), 1207 (sh), 1162 (m), 1077 (m), 1020 (m), 973 (w), 849 (m), 834 (m), 673 (sh), 657 (m), 614 (m).

Crystallographic details

For complete details pertaining to the single-crystal X-ray diffraction data for U(hfa)₄ and Th(hfa)₄(dme), refer to the ESI.†

Powder X-ray diffraction

Samples of COF-5, Th(hfa)₄@COF-5 and U(hfa)₄@COF-5 were prepared for data collection in transmission geometry by flame-sealing 0.7 mm quartz capillaries that had been packed with analyte in a glove-box. Samples of ThO₂ NPs@COF-5 and UO₂ NPs@COF-5 were prepared for data collection in reflection geometry by applying the powder directly to a silicon zero background plate, which was then covered with a thin Kapton film to provide an atmospheric barrier and containment for the radioactivity. Powder X-ray diffraction (PXRD) patterns were measured with either a Co source (40 kV, 40 mA) or Cu source (45 kV, 40 mA) by using a Panalytical X'Pert Pro diffractometer equipped with a focusing mirror, 0.02 radian Soller slits, and silicon strip detector. All data is presented as 2 θ plots for Cu K α X-rays. Data were obtained at room temperature as 12–24 scans with a counting time of approximately 2 hours per scan and 0.02° 2 θ step size, which were averaged using X'Pert High Score Plus software.

Transmission electron microscopy

TEM and high-angle annular dark-field (HAADF)-STEM images were collected on a JEOL 2100-F field emission TEM with an operating voltage of 120 kV. Samples for TEM were prepared by dispersing particles in hexane and drop casting onto copper TEM grids coated with carbon mesh and dried under vacuum. Focus was optimized using a particle on the edge of a NP-COF construct where thickness was minimal. Size analysis was performed by digitally measuring the width of nanocrystals; only particles showing substantial contrast from their COF template were counted for maximum accuracy. A sample size of 100 nanocrystals was used in both the case of ThO₂ NPs@COF-5 and UO₂ NPs@COF-5 to give a reasonable statistical distribution of nanocrystal size.



X-ray scattering

Small and wide angle X-ray scattering (SAXS and WAXS) patterns were collected at beamline 7.3.3 of the Advanced Light Source (ALS).¹⁷³ Data were collected at an incident energy of 10 keV using a Pilatus 2M detector and a beam size of 300 $\mu\text{m} \times 700 \mu\text{m}$. Samples were prepared for measurement by mixing with boron nitride and placing them in 1.5 mm-diameter quartz capillaries sealed with epoxy. The capillaries were placed into Kapton tubes with epoxy at both ends and taped into an aluminum sample holder sealed with Kapton windows. Data was azimuthally averaged and 1D plots extracted using the NIKA¹⁷⁴ software package in IGOR Pro. Data was then fit across the data collection range (between 0.1 and 1 \AA^{-1}) using the SciPy package¹⁷⁵ in Python to the analytical solution for a spherical form factor integrated over a Schulz distribution¹⁷⁶ along with background contributions. Backgrounds included Kapton, quartz, COF-5, the inclusion compound and boron nitride (see ESI† for additional information on backgrounds). Background patterns were fit in linear combination with the form factor, due to the variability in capillary thickness and sample packing density. Best-fit values were determined through minimization of χ^2 and error bars were determined to one standard deviation.

Soft X-ray spectromicroscopy

Sample preparation methodology for the potentially oxygen and moisture-sensitive analytes was similar to that described previously.^{177,178} Samples were prepared in an argon-filled glovebox by grinding the analyte into a fine powder with a mortar and pestle, and brushing the powder onto a Si_3N_4 membrane (100 nm, Silson) with a fiber. This method arranged a large number of micron-scale particles in a relatively compact area that were suitable for C, O, and F K-edge as well as actinide $\text{N}_{5,4}^-$ -edge measurements. A second membrane was placed over the sample, and the edges were sealed together using Hardman Double/Bubble® 5 minute epoxy.

Data acquisition methodology was similar to that discussed previously.¹⁷⁸ Single-energy images and spectra were acquired using both the STXM instruments at the Canadian Light Source (CLS) spectromicroscopy beamline 10ID-1 and at the Advanced Light Source-Molecular Environmental Science (ALS-MES) beamline 11.0.2. The CLS operated in decay mode (250 to 150 mA) and the ALS operated in topoff mode (500 mA). At both facilities, the beamlines operated with a ~ 0.5 atm He-filled chamber and used elliptically polarizing undulators that delivered photons to entrance slit-less plane-grating monochromators.¹⁷⁹⁻¹⁸² The maximum energy resolution $E/\Delta E$ approaches 7000 for both beamlines.^{179,180} Energy calibrations were performed at the C K-edge using CO_2 gas (C 1s \rightarrow 3p at 294.95 eV), the O K-edge using CO_2 gas (O 1s \rightarrow 3p at 538.9 eV), and at the F K-, Th $\text{N}_{5,4}^-$, and U $\text{N}_{5,4}^-$ -edges using Ne gas at the ALS (Ne 1s \rightarrow 3p at 867.30 eV) and SF_6 gas at the CLS (F 1s \rightarrow a_{1g} at 688.0 eV). For these measurements, the X-ray beam was focused with a 35 or 40 nm zone plate onto the sample, and the transmitted light was detected. Images at a single energy were obtained by raster-scanning the sample and collecting transmitted monochromatic light as a function of sample position.

Spectra at particular regions of interest on the sample image were extracted from the “stack”, which is a collection of images recorded at multiple, closely spaced photon energies across the absorption edge. Dwell times used to acquire an image at a single photon energy were typically 2 ms per pixel. C and O K-edge spectra were collected using circularly polarized radiation, while F K-, Th $\text{N}_{5,4}^-$, and U $\text{N}_{5,4}^-$ -edge measurements were collected using linearly polarized radiation. To evaluate the absorbance signal, the measured transmitted intensity (I) was converted to optical density (OD) using Beer-Lambert's law: $OD = \ln(I/I_0) = \mu\rho d$, where I_0 is the incident photon flux intensity, d is the sample thickness, and μ and ρ are the mass absorption coefficient and density of the sample material, respectively. Incident photon intensity was measured through the sample-free region of the Si_3N_4 windows. C K-, O K-, and F K-edge data were background-subtracted in MATLAB using the MBACK algorithm.¹⁸³ For Th $\text{N}_{5,4}^-$ and U $\text{N}_{5,4}^-$ -edge data, IGOR Pro 7 was used to fit a line to the pre-edge region, and then the line was subtracted from the experimental data to eliminate the background of the spectrum. IGOR Pro 7 was used for all XAS data to calculate second-derivative spectra which were used as guides to determine the number and position of peaks.

Reasonable efforts were made to minimize the effects of self-absorption and saturation by omitting thicker particles and ensuring that the spectra were governed by the Beer-Lambert law. Because these effects can be difficult to quantify,¹⁸⁴ and because of the different compositions and concentrations of the analytes, direct and quantitative comparisons cannot be made between the observed intensity of features observed in Fig. S10–S12.† Hence, the overall spectral profile and peak positions were to assess the presence or absence of transitions associated with particular chemical components or functional groups, in analogy to the “fingerprint” analysis used in IR spectroscopy.

X-ray absorption fine structure spectroscopy

Th and U XAFS spectra at their L_3 -edges (16.3 and 17.166 keV, respectively) were collected at Beamline 11-2 at the Stanford Synchrotron Radiation Lightsource using a Si 220 ($\varphi = 0$) monochromator detuned to 50%. Data were collected in both transmission and fluorescence mode, using a 100 Element Canberra Ge fluorescence detector (sample at 45° from the incident beam and fluorescence detector). No photoreduction of the sample was observed over time in the X-ray beam. Data were edge-energy calibrated using the first inflection point in the spectra of Zr foil (17 998 eV) and UO_2 (17 170 eV) standards. A slit height for the sample was chosen to be less than 0.7 mm, such that the data resolution would be core-hole lifetime limited.¹²⁶ Fluorescence data were also corrected for dead time. Data were reduced and analyzed using the RSXAP software package.^{125,126} Data were fit in r -space using EXAFS standards calculated using FEFF¹⁸⁵ and error bars calculated using a profiling method.¹⁸⁶ The number of parameters used in the fit were limited to be fewer than the number of independent points.

Powder samples were prepared for measurements through dilution with dry boron nitride and mixing using a mortar and



pestle in an argon-filled glovebox. The diluted samples were then packed into aluminum holders sealed with indium. Due to the air and water sensitivity of the samples, they were stored under argon until measurement. The sealed holders were exposed to air for less than one minute while being transferred to vacuum with an He backfill. Samples were measured using a liquid He-cooled cryostat to test for structural temperature dependence by collecting data either at 50 K and 300 K or in a series of 50 K, 100 K, 200 K and 300 K for Einstein-model analysis.¹³⁵

Author contributions

Moreau, Herve, Booth and Minasian conceived of the project and designed the experiments. The synthetic work and initial characterization by PXRD, NMR, and IR spectroscopy was performed by Herve, Braun, Liu, Russo, and Minasian. Lohrey and Teat did single-crystal XRD measurements and analysis, Straub and Alayoglu did TEM measurements and analysis, and Braun and Minasian did the STXM measurements and analysis. Moreau collected SAXS patterns and analyzed the data using Python code for SAXS data analysis developed by Booth and Moreau. Moreau, Deblonde, Olive, Qiao, Booth, and Minasian collected XAFS data and Moreau and Booth analyzed the data. The manuscript was written by Moreau, Herve, Minasian, and Booth, and reviewed by all authors.

Conflicts of interest

There are no conflicts to declare.

Acknowledgements

This work was supported by the Director, Office of Science, Office of Basic Energy Sciences, Division of Chemical Sciences, Geosciences, and Biosciences Heavy Element Chemistry Program of the U.S. Department of Energy (DOE) at LBNL under Contract No. DE-AC02-05CH11231. XAFS work was performed at the Stanford Synchrotron Radiation Lightsource, which is supported by the U.S. Department of Energy, Office of Science, Office of Basic Energy Sciences under contract no. DE-AC02-76SF00515. STXM research described in this paper was conducted at the Canadian Light Source, which is supported by the Canada Foundation for Innovation, Natural Sciences and Engineering Research Council of Canada, the University of Saskatchewan, the Government of Saskatchewan, Western Economic Diversification Canada, the National Research Council Canada, and the Canadian Institutes of Health Research. Additional STXM research was done at ALS beamline 11.0.2, SAXS work done at beamline 7.3.3, and X-ray crystallography work done at ALS beamline 11.3.1, which were supported by the Director of the Office of Science, Office of Basic Energy Sciences, of the U.S. Department of Energy under Contract No. DE-AC02-05CH11231. TEM work at the Molecular Foundry was supported by the Office of Science, Office of Basic Energy Sciences, of the U.S. Department of

Energy under Contract No. DE-AC02-05CH11231. D. Olive was supported by the Los Alamos National Laboratory (LANL) LDRD Program and the Glenn T. Seaborg Institute for Transactinium Science. LANL is operated by Triad National Security, LLC, for the National Nuclear Security Administration of the U.S. Department of Energy (Contract No. 89233218CNA000001). Preliminary TEM measurements were also performed using EMSL, a DOE Office of Science User Facility sponsored by the Office of Biological and Environmental Research. We would like to thank Eric Schaible, Chenhui Zhu and Alexander Liebman-Pelaez for their assistance with SAXS measurements, Maria Altoe, Shaul Aloni and Libor Kovarik for assistance with TEM, and Ryan Davis for his assistance with XAFS measurements.

References

- 1 J. Spino, H. Santa Cruz, R. Jovani-Abril, R. Birtcher and C. Ferrero, *J. Nucl. Mater.*, 2012, **422**, 27–44.
- 2 T. M. Nenoff, B. W. Jacobs, D. B. Robinson, P. P. Provencio, J. Huang, S. Ferreira and D. J. Hanson, *Chem. Mater.*, 2011, **23**, 5185–5190.
- 3 M. Amaya, J. Nakamura and T. Fuketa, *J. Nucl. Sci. Technol.*, 2008, **45**, 244–250.
- 4 Q. Yin, A. Kutepov, K. Haule, G. Kotliar, S. Y. Savrasov and W. E. Pickett, *Phys. Rev. B: Condens. Matter Mater. Phys.*, 2011, **84**, 195111.
- 5 V. V. Rondinella and T. Wiss, *Mater. Today*, 2010, **13**, 24–32.
- 6 C. Ronchi, M. Sheindlin, D. Staicu and M. Kinoshita, *J. Nucl. Mater.*, 2004, **327**, 58–76.
- 7 B. A. Powell, Z. Dai, M. Zavarin, P. Zhao and A. B. Kersting, *Environ. Sci. Technol.*, 2011, **45**, 2698–2703.
- 8 A. Y. Romanchuk, S. N. Kalmykov, A. V. Egorov, Y. V. Zubavichus, A. A. Shiryayev, O. N. Batuk, S. D. Conradson, D. A. Pankratov and I. A. Presnyakov, *Geochim. Cosmochim. Acta*, 2013, **121**, 29–40.
- 9 T. Parsons-Moss, H. Tuysuz, D. Wang, S. Jones, D. Olive and H. Nitsche, *Radiochim. Acta*, 2014, **102**, 489–504.
- 10 J. I. Kim, *MRS Bull.*, 1994, **19**, 47–53.
- 11 D. L. Clark, G. R. Choppin, C. S. Dayton, D. R. Janecky, L. J. Lane and I. Paton, *J. Alloys Compd.*, 2007, **444–445**, 11–18.
- 12 J. Jeon, *Int. J. Mol. Sci.*, 2019, **20**, 2323.
- 13 G. Song, L. Cheng, Y. Chao, K. Yang and Z. Liu, *Adv. Mater.*, 2017, **29**, 1700996.
- 14 N. A. Thiele and J. J. Wilson, *Cancer Biother. Radiopharm.*, 2018, **33**, 336–348.
- 15 E. Cędrowska, M. Pruszynski, A. Majkowska-Pilip, S. Męczyńska-Wielgosz, F. Bruchertseifer, A. Morgenstern and A. Bilewicz, *J. Nanopart. Res.*, 2018, **20**, 83.
- 16 M. F. McLaughlin, J. Woodward, R. Boll, J. Wall, A. Rondinone, S. Kennel, S. Mirzadeh and D. J. Robertson, *PLoS One*, 2013, **8**, e54531.
- 17 M. Toro Gonzalez, A. Dame, S. Mirzadeh and J. Rojas, *J. Appl. Phys.*, 2019, **125**, 214901.
- 18 H. Wu, Y. Yang and Y. C. Cao, *J. Am. Chem. Soc.*, 2006, **128**, 16522–16523.



19 J. Leduc, M. Frank, L. Jürgensen, D. Graf, A. Raauf and S. Mathur, *ACS Catal.*, 2019, **9**, 4719–4741.

20 M. D. Straub, J. Leduc, M. Frank, A. Raauf, T. D. Lohrey, S. G. Minasian, S. Mathur and J. Arnold, *Angew. Chem., Int. Ed.*, 2019, **58**, 5749–5753.

21 J. Leduc, J. I. Pacold, D. K. Shuh, C.-L. Dong and S. Mathur, *J. Inorg. Gen. Chem.*, 2018, **644**, 12–18.

22 L. Appel, J. Leduc, C. L. Webster, J. W. Ziller, W. J. Evans and S. Mathur, *Angew. Chem., Int. Ed.*, 2015, **54**, 2209–2213.

23 S. Hu, H. Li, H. Liu, P. He and X. Wang, *Small*, 2015, **11**, 2624–2630.

24 Z. T. Zhang, M. Konduru, S. Dai and S. H. Overbury, *Chem. Commun.*, 2002, **20**, 2406–2407.

25 D. V. Talapin, J.-S. Lee, M. V. Kovalenko and E. V. Shevchenko, *Chem. Rev.*, 2010, **110**, 389–458.

26 M. A. Boles, D. Ling, T. Hyeon and D. V. Talapin, *Nat. Mater.*, 2016, **15**, 141.

27 A. Henglein, *Chem. Rev.*, 1989, **89**, 1861–1873.

28 G. M. Whitesides, *Small*, 2005, **1**, 172–179.

29 A. P. Alivisatos, *J. Phys. Chem.*, 1996, **100**, 13226–13239.

30 S. N. Kalmykov and M. A. Denecke, *Actinide Nanoparticle Research*, Springer, New York, 2011.

31 C. Falaise, H. A. Neal and M. Nyman, *Inorg. Chem.*, 2017, **56**, 6591–6598.

32 G. X. Wang, E. R. Batista and P. Yang, *Phys. Chem. Chem. Phys.*, 2018, **20**, 17563–17573.

33 P. Miro, B. Vlaisavljevich, A. L. Dzubak, S. X. Hu, P. C. Burns, C. J. Cramer, R. Spezia and L. Gagliardi, *J. Phys. Chem. C*, 2014, **118**, 24730–24740.

34 S. O. Odoh, J. Shamblin, C. A. Colla, S. Hickam, H. L. Lobeck, R. A. K. Lopez, T. Olds, J. E. S. Szymanowski, G. E. Sigmon, J. Neufeld, W. H. Casey, M. Lang, L. Gagliardi and P. C. Burns, *Inorg. Chem.*, 2016, **55**, 3541–3546.

35 M. V. Ryzhkov, A. Mirmelstein, B. Delley, S. W. Yu, B. W. Chung and J. G. Tobin, *J. Electron Spectrosc. Relat. Phenom.*, 2014, **194**, 45–56.

36 M. V. Ryzhkov, A. Mirmelstein, S.-W. Yu, B. W. Chung and J. G. Tobin, *Int. J. Quantum Chem.*, 2013, **113**, 1957–1965.

37 J. Park, J. Joo, S. G. Kwon, Y. Jang and T. Hyeon, *Angew. Chem., Int. Ed.*, 2007, **46**, 4630–4660.

38 M. L. Neidig, D. L. Clark and R. L. Martin, *Coord. Chem. Rev.*, 2013, **257**, 394–406.

39 K. T. Moore and G. van der Laan, *Rev. Mod. Phys.*, 2009, **81**, 235–298.

40 G. R. Stewart, *Rev. Mod. Phys.*, 1984, **56**, 755–787.

41 E. D. Bauer and J. D. Thompson, *Annu. Rev. Condens. Matter Phys.*, 2015, **6**, 137–153.

42 J. G. Tobin and S. W. Yu, *Phys. Rev. Lett.*, 2011, **107**, 167406.

43 J. G. Tobin, S. W. Yu, R. Qiao, W. L. Yang, C. H. Booth, D. K. Shuh, A. M. Duffin, D. Sokaras, D. Nordlund and T. C. Weng, *Phys. Rev. B: Condens. Matter Mater. Phys.*, 2015, **92**, 045130.

44 S. E. Gilson, P. Li, J. E. S. Szymanowski, J. White, D. Ray, L. Gagliardi, O. K. Farha and P. C. Burns, *J. Am. Chem. Soc.*, 2019, **141**, 11842–11846.

45 J. Qiu and P. C. Burns, *Chem. Rev.*, 2013, **113**, 1097–1120.

46 C. Tamain, T. Dumas, D. Guillaumont, C. Hennig and P. Guibaud, *Eur. J. Inorg. Chem.*, 2016, **2016**, 3536–3540.

47 O. A. Ejegbawo, C. R. Martin, O. A. Olorunfemi, G. A. Leith, R. T. Ly, A. M. Rice, E. A. Dolgopolova, M. D. Smith, S. G. Karakalos, N. Birkner, B. A. Powell, S. Pandey, R. J. Koch, S. T. Misture, H.-C. z. Loyer, S. R. Phillipot, K. S. Brinkman and N. B. Shustova, *J. Am. Chem. Soc.*, 2019, **141**, 11628–11640.

48 E. A. Dolgopolova, A. M. Rice and N. B. Shustova, *Chem. Commun.*, 2018, **54**, 6472–6483.

49 P. O. Adelani and T. E. Albrecht-Schmitt, *Angew. Chem., Int. Ed.*, 2010, **49**, 8909–8911.

50 S. Wu, S. Wang, J. Diwu, W. Depmeier, T. Malcherek, E. V. Alekseev and T. E. Albrecht-Schmitt, *Chem. Commun.*, 2012, **48**, 3479–3481.

51 P. C. Burns, K.-A. Kubatko, G. Sigmon, B. J. Fryer, J. E. Gagnon, M. R. Antonio and L. Soderholm, *Angew. Chem., Int. Ed.*, 2005, **44**, 2135–2139.

52 A. Gil, D. Karhánek, P. Miró, M. R. Antonio, M. Nyman and C. Bo, *Chem.-Eur. J.*, 2012, **18**, 8340–8346.

53 E. J. Schofield, H. Veeramani, J. O. Sharp, E. Suvorova, R. Bernier-Latmani, A. Mehta, J. Stahlman, S. M. Webb, D. L. Clark, S. D. Conradson, E. S. Ilton and J. R. Bargar, *Environ. Sci. Technol.*, 2008, **42**, 7898–7904.

54 J. C. Berthet, P. Thuery and M. Ephritikhine, *Inorg. Chem.*, 2010, **49**, 8173–8177.

55 M. Basile, D. K. Unruh, K. Gojdas, E. Flores, L. Streicher and T. Z. Forbes, *Chem. Commun.*, 2015, **51**, 5306–5309.

56 J. C. Berthet, P. Thuery and M. Ephritikhine, *Angew. Chem., Int. Ed.*, 2008, **47**, 5586–5589.

57 C. Falaise, C. Volkringer, C. Hennig and T. Loiseau, *Chem.-Eur. J.*, 2015, **21**, 16654–16664.

58 C. Falaise, C. Volkringer, J. F. Vigier, A. Beaurain, P. Roussel, P. Rabu and T. Loiseau, *J. Am. Chem. Soc.*, 2013, **135**, 15678–15681.

59 G. Nocton, F. Burdet, J. Pecaut and M. Mazzanti, *Angew. Chem., Int. Ed.*, 2007, **46**, 7574–7578.

60 X. Y. Qian, T. H. Zhou and J. G. Mao, *Dalton Trans.*, 2015, **44**, 13573–13580.

61 L. Salmon, P. Thuery and M. Ephritikhine, *Polyhedron*, 2004, **23**, 623–627.

62 K. E. Knope and L. Soderholm, *Inorg. Chem.*, 2013, **52**, 6770–6772.

63 K. E. Knope, M. Vasiliu, D. A. Dixon and L. Soderholm, *Inorg. Chem.*, 2012, **51**, 4239–4249.

64 L. Soderholm, P. M. Almond, S. Skanthakumar, R. E. Wilson and P. C. Burns, *Angew. Chem., Int. Ed.*, 2008, **47**, 298–302.

65 L. Chatelain, R. Faizova, F. Fadaei-Tirani, J. Pecaut and M. Mazzanti, *Angew. Chem., Int. Ed.*, 2019, **58**, 3021–3026.

66 G. E. Sigmon and A. E. Hixon, *Chem.-Eur. J.*, 2019, **25**, 2463–2466.

67 M. C. Rath, S. J. Keny and D. B. Naik, *Radiat. Phys. Chem.*, 2016, **126**, 85–89.

68 S. I. Nikitenko, P. Moisy, P. Blanc and C. Madic, *Cron. Chim.*, 2004, **7**, 1191–1199.



69 E. Dalodiere, M. Virot, V. Morosini, T. Chave, T. Dumas, C. Hennig, T. Wiss, O. D. Blanco, D. K. Shuh, T. Tyliszczak, L. Venault, P. Moisy and S. I. Nikitenko, *Sci. Rep.*, 2017, **7**, 43514.

70 P. Chen, D. Y. Huang, C. C. Chen, T. Suzuki-Muresan, M. L. Kang, J. Wang, G. Song and B. A. Wang, *J. Radioanal. Nucl. Chem.*, 2017, **313**, 229–237.

71 R. Zhao, L. Wang, Z. J. Gu, L. Y. Yuan, C. L. Xiao, Y. L. Zhao, Z. F. Chai and W. Q. Shi, *CrystEngComm*, 2014, **16**, 2645–2651.

72 D. Hudry, C. Apostolidis, O. Walter, T. Gouder, E. Courtois, C. Kuebel and D. Meyer, *Chem.-Eur. J.*, 2012, **18**, 8283–8287.

73 D. Hudry, C. Apostolidis, O. Walter, T. Gouder, E. Courtois, C. Kuebel and D. Meyer, *Chem.-Eur. J.*, 2013, **19**, 5297–5305.

74 D. Hudry, C. Apostolidis, O. Walter, T. Gouder, A. Janssen, E. Courtois, C. Kuebel and D. Meyer, *RSC Adv.*, 2013, **3**, 18271–18274.

75 D. Hudry, C. Apostolidis, O. Walter, A. Janssen, D. Manara, J.-C. Griveau, E. Colineau, T. Vitova, T. Pruessmann, D. Wang, C. Kuebel and D. Meyer, *Chem.-Eur. J.*, 2014, **20**, 10431–10438.

76 D. Hudry, J.-C. Griveau, C. Apostolidis, O. Walter, E. Colineau, G. Rasmussen, D. Wang, V. S. K. Chakravadhaluna, E. Courtois, C. Kuebel and D. Meyer, *Nano Res.*, 2014, **7**, 119–131.

77 T. Rajh, L. X. Chen, K. Lukas, T. Liu, M. C. Thurnauer and D. M. Tiede, *J. Phys. Chem. B*, 2002, **106**, 10543–10552.

78 L. X. Chen, T. Liu, M. C. Thurnauer, R. Csencsits and T. Rajh, *J. Phys. Chem. B*, 2002, **106**, 8539–8546.

79 P. Zhang and T. K. Sham, *Appl. Phys. Lett.*, 2002, **81**, 736–738.

80 A. B. Altman, C. D. Pemmaraju, S. Alayoglu, J. Arnold, C. H. Booth, A. Braun, C. E. Bunker, A. Herve, S. G. Minasian, D. Prendergast, D. K. Shuh and T. Tyliszczak, *Inorg. Chem.*, 2017, **56**, 5710–5719.

81 D. Li, C. Wang, D. Tripkovic, S. Sun, N. M. Markovic and V. R. Stamenkovic, *ACS Catal.*, 2012, **2**, 1358–1362.

82 D. Ung and B. M. Cossairt, *ACS Appl. Energy Mater.*, 2019, **2**, 1642–1645.

83 X.-K. Wan, J.-Q. Wang, Z.-A. Nan and Q.-M. Wang, *Sci. Adv.*, 2017, **3**, e1701823.

84 A. M. Smith, H. Duan, M. N. Rhyner, G. Ruan and S. Nie, *Phys. Chem. Chem. Phys.*, 2006, **8**, 3895–3903.

85 C. Bullen and P. Mulvaney, *Langmuir*, 2006, **22**, 3007–3013.

86 A. M. Munro, I. Jen-La Plante, M. S. Ng and D. S. Ginger, *J. Phys. Chem. C*, 2007, **111**, 6220–6227.

87 M. Meilikhov, K. Yusenko, D. Esken, S. Turner, G. Van Tendeloo and R. A. Fischer, *Eur. J. Inorg. Chem.*, 2010, **24**, 3701–3714.

88 H. R. Moon, D.-W. Lim and M. P. Suh, *Chem. Soc. Rev.*, 2013, **42**, 1807–1824.

89 S. B. Kalidindi and R. A. Fischer, *Phys. Status Solidi B*, 2013, **250**, 1119–1127.

90 P. J. Waller, F. Gandara and O. M. Yaghi, *Acc. Chem. Res.*, 2015, **48**, 3053–3063.

91 M. S. Lohse and T. Bein, *Adv. Funct. Mater.*, 2018, **28**, 1705553.

92 P. Pachfule, M. K. Panda, S. Kandambeth, S. M. Shivaprasad, D. D. Diaz and R. Banerjee, *J. Mater. Chem. A*, 2014, **2**, 7944–7952.

93 S. L. Lu, Y. M. Hu, S. Wan, R. McCaffrey, Y. H. Jin, H. W. Gu and W. Zhang, *J. Am. Chem. Soc.*, 2017, **139**, 17082–17088.

94 H. Zhong, C. P. Liu, Y. X. Wang, R. H. Wang and M. C. Hong, *Chem. Sci.*, 2016, **7**, 2188–2194.

95 J. Zhao, D. G. Bachmann, M. Lenz, D. G. Gillingham and T. R. Ward, *Catal.: Sci. Technol.*, 2018, **8**, 2294–2298.

96 R. L. Wang, D. P. Li, L. J. Wang, X. Zhang, Z. Y. Zhou, J. L. Mu and Z. M. Su, *Dalton Trans.*, 2019, **48**, 1051–1059.

97 P. Pachfule, S. Kandambeth, D. D. Diaz and R. Banerjee, *Chem. Commun.*, 2014, **50**, 3169–3172.

98 X. F. Shi, Y. J. Yao, Y. L. Xu, K. Liu, G. S. Zhu, L. F. Chi and G. Lu, *ACS Appl. Mater. Interfaces*, 2017, **9**, 7481–7488.

99 A. P. Cote, A. I. Benin, N. W. Ockwig, M. O'Keeffe, A. J. Matzger and O. M. Yaghi, *Science*, 2005, **310**, 1166–1170.

100 M. Vasiliu, K. E. Knope, L. Soderholm and D. A. Dixon, *J. Phys. Chem. A*, 2012, **116**, 6917–6926.

101 B. Lukose, A. Kuc and T. Heine, *Chem.-Eur. J.*, 2011, **17**, 2388–2392.

102 L. M. Lanni, R. W. Tilford, M. Bharathy and J. J. Lavigne, *J. Am. Chem. Soc.*, 2011, **133**, 13975–13983.

103 M. Calik, T. Sick, M. Dogru, M. Döblinger, S. Datz, H. Budde, A. Hartschuh, F. Auras and T. Bein, *J. Am. Chem. Soc.*, 2016, **138**, 1234–1239.

104 D. Esken, H. Noei, Y. Wang, C. Wiktor, S. Turner, G. Van Tendeloo and R. A. Fischer, *J. Mater. Chem.*, 2011, **21**, 5907–5915.

105 J. Hafizovic, M. Bjørgen, U. Olsbye, P. D. C. Dietzel, S. Bordiga, C. Prestipino, C. Lamberti and K. P. Lillerud, *J. Am. Chem. Soc.*, 2007, **129**, 3612–3620.

106 W. D. Pyrz and D. J. Buttrey, *Langmuir*, 2008, **24**, 11350–11360.

107 F. Schroeder and R. A. Fischer, in *Functional Metal–Organic Frameworks: Gas Storage, Separation and Catalysis*, ed. M. Schroder, 2010, vol. 293, pp. 77–113.

108 S. Turner, O. I. Lebedev, F. Schröder, D. Esken, R. A. Fischer and G. V. Tendeloo, *Chem. Mater.*, 2008, **20**, 5622–5627.

109 M. Nyman, *Coord. Chem. Rev.*, 2017, **352**, 461–472.

110 C. Falaise, K. Kozma and M. Nyman, *Chem.-Eur. J.*, 2018, **24**, 14226–14232.

111 B. H. Kim, M. J. Hackett, J. Park and T. Hyeon, *Chem. Mater.*, 2014, **26**, 59–71.

112 V. L. Devito and D. W. Wester, *J. Inorg. Nucl. Chem.*, 1980, **42**, 1719–1723.

113 T. Yoshimura, C. Miyake and S. Imoto, *Bull. Chem. Soc. Jpn.*, 1973, **46**, 2096–2101.

114 K. W. Bagnall and M. W. Wakerley, *J. Inorg. Nucl. Chem.*, 1975, **37**, 329–330.

115 F. M. F. de Groot, E. de Smit, M. M. van Schooneveld, L. R. Aramburo and B. M. Weckhuysen, *ChemPhysChem*, 2010, **11**, 951–962.

116 K. D. Pollard, H. A. Jenkins and R. J. Puddephatt, *Chem. Mater.*, 2000, **12**, 701–710.



117 A. C. Jones, H. C. Aspinall, P. R. Chalker, R. J. Potter, K. Kukli, A. Rahtu, M. Ritala and M. Leskela, *Mater. Sci. Eng., B*, 2005, **118**, 97–104.

118 G. Malandrino and I. L. Fragala, *Coord. Chem. Rev.*, 2006, **250**, 1605–1620.

119 H. C. Aspinall, in *Rare Earth Oxide Thin Films: Growth, Characterization, and Applications*, ed. M. Fanciulli and G. Scarel, 2007, vol. 106, pp. 53–72.

120 S. R. Daly, D. Y. Kim and G. S. Girolami, *Inorg. Chem.*, 2012, **51**, 7050–7065.

121 S. R. Daly, D. Y. Kim, Y. Yang, J. R. Abelson and G. S. Girolami, *J. Am. Chem. Soc.*, 2010, **132**, 2106–2107.

122 M. C. Barry, Z. Wei, T. He, A. S. Filatov and E. V. Dikarev, *J. Am. Chem. Soc.*, 2016, **138**, 8883–8887.

123 S. Battiatto, P. Rossi, P. Paoli and G. Malandrino, *Inorg. Chem.*, 2018, **57**, 15035–15039.

124 R. Lessard, J. Cuny, G. Cooper and A. P. Hitchcock, *Chem. Phys.*, 2007, **331**, 289–303.

125 T. M. Hayes and J. B. Boyce, in *Solid State Phys.*, ed. H. Ehrenreich, F. Seitz and D. Turnbull, Academic Press, 1983, vol. 37, pp. 173–351.

126 G. G. Li, F. Bridges and C. H. Booth, *Phys. Rev. B: Condens. Matter Mater. Phys.*, 1995, **52**, 6332–6348.

127 E. J. Schelter, R. Wu, J. M. Veauthier, E. D. Bauer, C. H. Booth, R. K. Thomson, C. R. Graves, K. D. John, B. L. Scott, J. D. Thompson, D. E. Morris and J. L. Kiplinger, *Inorg. Chem.*, 2010, **49**, 1995–2007.

128 J. Rothe, C. Walther, M. A. Denecke and T. Fanghänel, *Inorg. Chem.*, 2004, **43**, 4708–4718.

129 J. Rothe, M. A. Denecke, V. Neck, R. Müller and J. I. Kim, *Inorg. Chem.*, 2002, **41**, 249–258.

130 L. Bonato, M. Virot, T. Dumas, A. Mesbah, E. Dalodiére, O. Dieste Blanco, T. Wiss, X. Le Goff, M. Odorico, D. Prieur, A. Rossberg, L. Venault, N. Dacheux, P. Moisy and S. I. Nikitenko, *Nanoscale Adv.*, 2020, **2**, 214–224.

131 D. Bazin, D. Sayers, J. J. Rehr and C. Mottet, *J. Phys. Chem. B*, 1997, **101**, 5332–5336.

132 L. Amidani, T. V. Plakhova, A. Y. Romanchuk, E. Gerber, S. Weiss, A. Efimenko, C. J. Sahle, S. M. Butorin, S. N. Kalmykov and K. O. Kvashnina, *Phys. Chem. Chem. Phys.*, 2019, **21**, 10635–10643.

133 S. Calvin, C. J. Riedel, E. E. Carpenter, S. A. Morrison, R. M. Stroud and V. G. Harris, *Phys. Scr.*, 2005, **T115**, 744–748.

134 E. Sevillano, H. Meuth and J. J. Rehr, *Phys. Rev. B: Condens. Matter Mater. Phys.*, 1979, **20**, 4908–4911.

135 E. D. Crozier, J. J. Rehr and R. Ingalls, in *X-Ray Absorption: Principles, Applications, Techniques of EXAFS, SEXAFS, XANES*, ed. D. Konginsberger and R. Prins, Wiley, New York, 1988, ch. 373, p. 373.

136 C. H. Booth, F. Bridges, G. H. Kwei, J. M. Lawrence, A. L. Cornelius and J. J. Neumeier, *Phys. Rev. B: Condens. Matter Mater. Phys.*, 1998, **57**, 10440–10454.

137 C. Tamain, T. Dumas, C. Hennig and P. Guilbaud, *Chem.-Eur. J.*, 2017, **23**, 6864–6875.

138 J. J. Rehr, C. H. Booth, F. Bridges and S. I. Zabinsky, *Phys. Rev. B: Condens. Matter Mater. Phys.*, 1994, **49**, 12347–12350.

139 G. E. v. Dorssen, D. C. Koningsberger and D. E. Ramaker, *J. Phys.: Condens. Matter*, 2002, **14**, 13529–13541.

140 D. E. Keller, B. M. Weckhuysen and D. C. Koningsberger, *Chem.-Eur. J.*, 2007, **13**, 5845–5856.

141 H. Wende, C. Litwinski, A. Scherz, T. Gleitsmann, Z. Li, C. Sorg, K. Baberschke, A. Ankudinov, J. J. Rehr and C. Jung, *J. Phys.: Condens. Matter*, 2003, **15**, 5197–5206.

142 M. S. Wickleder, B. Fourest and P. K. Dorhout, in *The Chemistry of the Actinide and Transactinide Elements*, ed. L. L. Morss, N. Edelstein and J. Fuger, Springer, Berlin, 2006, vol. 1ch. 3, pp. 52–160.

143 G. Leinders, J. Pakarinen, R. Delville, T. Cardinaels, K. Binnemans and M. Verwerft, *Inorg. Chem.*, 2016, **55**, 3915–3927.

144 T. Yao, K. Mo, D. Yun, S. Nanda, A. M. Yacout and J. Lian, *J. Am. Ceram. Soc.*, 2017, **100**, 2651–2658.

145 S. D. Conradson, B. D. Begg, D. L. Clark, C. den Auwer, M. Ding, P. K. Dorhout, F. J. Espinosa-Faller, P. L. Gordon, R. G. Haire, N. J. Hess, R. F. Hess, D. Webster Keogh, G. H. Lander, D. Manara, L. A. Morales, M. P. Neu, P. Paviet-Hartmann, J. Rebizant, V. V. Rondinella, W. Runde, C. Drew Tait, D. Kirk Veirs, P. M. Villella and F. Wastin, *J. Solid State Chem.*, 2005, **178**, 521–535.

146 I. Grenthe, J. Drozdynski, T. Fujino, E. C. Buck, T. E. Albrecht-Schmitt and S. F. Wolf, in *The Chemistry of the Actinide and Transactinide Elements*, ed. L. R. Morss, N. M. Edelstein and J. Fuger, Springer, Berlin, 2006, vol. 1, p. 253.

147 S. E. Bone, J. J. Dynes, J. Cliff and J. R. Bargar, *Proc. Natl. Acad. Sci. U. S. A.*, 2017, **114**, 711–716.

148 V. Noël, K. Boye, J. S. Lezama Pacheco, S. E. Bone, N. Janot, E. Cardarelli, K. H. Williams and J. R. Bargar, *Environ. Sci. Technol.*, 2017, **51**, 10954–10964.

149 F. N. Skomurski, J. W. Wang, R. C. Ewing and U. Becker, *J. Nucl. Mater.*, 2013, **434**, 422–433.

150 Y. Yin and A. P. Alivisatos, *Nature*, 2005, **437**, 664–670.

151 J. D. Padmos, M. L. Personick, Q. Tang, P. N. Duchesne, D.-e. Jiang, C. A. Mirkin and P. Zhang, *Nat. Commun.*, 2015, **6**, 7664.

152 S. J. Hurst, A. K. R. Lytton-Jean and C. A. Mirkin, *Anal. Chem.*, 2006, **78**, 8313–8318.

153 D. T. Olive, D. L. Wang, C. H. Booth, E. D. Bauer, A. L. Pugmire, F. J. Freibert, S. K. McCall, M. A. Wall and P. G. Allen, *J. Appl. Phys.*, 2016, **120**, 035103.

154 S. Calvin, S. X. Luo, C. Caragianis-Broadbridge, J. K. McGuinness, E. Anderson, A. Lehman, K. H. Wee, S. A. Morrison and L. K. Kurihara, *Appl. Phys. Lett.*, 2005, **87**, 233102.

155 E. N. Hodkin and M. G. Nicholas, *J. Nucl. Mater.*, 1977, **67**, 171–180.

156 P. W. Tasker, *Surf. Sci.*, 1979, **87**, 315–324.

157 H. Idriss, *Surf. Sci. Rep.*, 2010, **65**, 67–109.

158 B. Biswas, V. Mougel, J. Pecaut and M. Mazzanti, *Angew. Chem., Int. Ed.*, 2011, **50**, 5744–5747.

159 K. S. Suslick, S.-B. Choe, A. A. Cichowlas and M. W. Grinstaff, *Nature*, 1991, **353**, 414.



160 O. Delmer, P. Balaya, L. Kienle and J. Maier, *Adv. Mater.*, 2008, **20**, 501–505.

161 G. Kumar, H. X. Tang and J. Schroers, *Nature*, 2009, **457**, 868.

162 A. H. Tavakoli, P. S. Maram, S. J. Widgeon, J. Rufner, K. van Benthem, S. Ushakov, S. Sen and A. Navrotsky, *J. Phys. Chem. C*, 2013, **117**, 17123–17130.

163 Y. Kawabata, K. Wada, M. Nakatani, S. Yamada and S. Onoue, *Int. J. Pharm.*, 2011, **420**, 1–10.

164 T. Sonoda, M. Kinoshita, I. L. F. Ray, T. Wiss, H. Thiele, D. Pellottiero, V. V. Rondinella and H. Matzke, *Nucl. Instrum. Methods Phys. Res., Sect. B*, 2002, **191**, 622–628.

165 T. Sonoda, M. Kinoshita, N. Ishikawa, M. Satake, A. Iwase and K. Yasunaga, *Nucl. Instrum. Methods Phys. Res., Sect. B*, 2010, **268**, 3277–3281.

166 J. Noirot, L. Desgranges and J. Lamontagne, *J. Nucl. Mater.*, 2008, **372**, 318–339.

167 W. J. Weber, *Radiat. Eff.*, 1984, **83**, 145–156.

168 W. J. Weber, R. C. Ewing, C. R. A. Catlow, T. Diaz de la Rubia, L. W. Hobbs, C. Kinoshita, H. Matzke, A. T. Motta, M. Nastasi, E. K. H. Salje, E. R. Vance and S. J. Zinkle, *J. Mater. Res.*, 1998, **13**, 1434–1484.

169 P. Makowski, X. Deschanel, A. Grandjean, D. Meyer, G. Toquer and F. Goettmann, *New J. Chem.*, 2012, **36**, 531–541.

170 B. J. Smith and W. R. Dichtel, *J. Am. Chem. Soc.*, 2014, **136**, 8783–8789.

171 J. M. Berg, D. L. Clark, J. C. Huffman, D. E. Morris, A. P. Sattelberger, W. E. Streib, W. G. Van der Sluys and J. G. Watkin, *J. Am. Chem. Soc.*, 1992, **114**, 10811–10821.

172 S. D. Conradson, T. Durakiewicz, F. J. Espinosa-Faller, Y. Q. An, D. A. Andersson, A. R. Bishop, K. S. Boland, J. A. Bradley, D. D. Byler, D. L. Clark, D. R. Conradson, L. L. Conradson, A. L. Costello, N. J. Hess, G. H. Lander, A. Llobet, M. B. Martucci, J. Mustre de Leon, D. Nordlund, J. S. Lezama-Pacheco, T. E. Proffen, G. Rodriguez, D. E. Schwarz, G. T. Seidler, A. J. Taylor, S. A. Trugman, T. A. Tyson and J. A. Valdez, *Phys. Rev. B: Condens. Matter Mater. Phys.*, 2013, **88**, 115135.

173 A. Hexemer, W. Bras, J. Glossinger, E. Schaible, E. Gann, R. Kirian, A. MacDowell, M. Church, B. Rude and H. Padmore, *J. Phys.: Conf. Ser.*, 2010, **247**, 012007.

174 J. Ilavsky, *J. Appl. Crystallogr.*, 2012, **45**, 324–328.

175 E. Jones, T. Oliphant and others, *SciPy: Open Source Scientific Tools for Python*, 2001, <http://www.scipy.org/>.

176 M. Kotlarchyk and S.-H. Chen, *J. Chem. Phys.*, 1983, **79**, 2461–2469.

177 A. B. Altman, C. D. Pemmaraju, C. Camp, J. Arnold, S. G. Minasian, D. Prendergast, D. K. Shuh and T. Tyliszczak, *J. Am. Chem. Soc.*, 2015, **137**, 10304–10316.

178 A. B. Altman, J. I. Pacold, J. Wang, W. W. Lukens and S. G. Minasian, *Dalton Trans.*, 2016, **45**, 9948–9961.

179 K. V. Kaznatcheev, C. Karunakaran, U. D. Lanke, S. G. Urquhart, M. Obst and A. P. Hitchcock, *Nucl. Instrum. Methods Phys. Res., Sect. A*, 2007, **582**, 96–99.

180 H. Bluhm, K. Andersson, T. Araki, K. Benzerara, G. E. Brown, J. J. Dynes, S. Ghosal, M. K. Gilles, H. C. Hansen, J. C. Hemminger, A. P. Hitchcock, G. Ketteler, A. L. D. Kilcoyne, E. Kneedler, J. R. Lawrence, G. G. Leppard, J. Majzlam, B. S. Mun, S. C. B. Myneni, A. Nilsson, H. Ogasawara, D. F. Ogletree, K. Pecher, M. Salmeron, D. K. Shuh, B. Tonner, T. Tyliszczak, T. Warwick and T. H. Yoon, *J. Electron Spectrosc. Relat. Phenom.*, 2006, **150**, 86–104.

181 H. J. Nilsson, T. Tyliszczak, R. E. Wilson, L. Werme and D. K. Shuh, *Anal. Bioanal. Chem.*, 2005, **383**, 41–47.

182 T. Tyliszczak, T. Warwick, A. L. D. Kilcoyne, S. Fakra, D. K. Shuh, T. H. Yoon, G. E. Brown Jr, S. Andrews, V. Chembrolu, J. Strachan and Y. Acremann, *AIP Conf. Proc.*, 2004, **705**, 1356–1359.

183 T.-C. Weng, G. S. Waldo and J. E. Penner-Hahn, *J. Synchrotron Radiat.*, 2004, **12**, 506–510.

184 S. Hanhan, A. M. Smith, M. Obst and A. P. Hitchcock, *J. Electron Spectrosc. Relat. Phenom.*, 2009, **173**, 44–49.

185 A. L. Ankudinov, B. Ravel, J. J. Rehr and S. D. Conradson, *Phys. Rev. B: Condens. Matter Mater. Phys.*, 1998, **58**, 7565–7576.

186 C. H. Booth and Y.-J. Hu, *J. Phys.: Conf. Ser.*, 2009, **190**, 012028.

